Electronic Supplementary Material (ESI) for ChemComm.

ELECTRONIC SUPPLEMENTARY INFORMATION

Chemical and *in silico* tuning of the magnetisation reversal barrier in pentagonal bipyramidal Dy(III) single-ion magnets

Angelos B. Canaj,[a] Mukesh Kumar Singh[b], Claire Wilson[a], Gopalan Rajaraman*[b] and Mark Murrie*[a]

[a] WestCHEM, School of Chemistry, University of Glasgow, University Avenue, Glasgow, G12 8QQ, UK.E-mail: Mark.Murrie@glasgow.ac.uk

[b] Department of Chemistry, Indian Institute of Technology Bombay, Powai, Mumbai, Maharashtra, 400076, India. E-mail: rajaraman@chem.iitb.ac.in

Materials and physical measurements

All manipulations were performed under aerobic conditions, using materials as received. Elemental analyses (C, H, N) were performed by the University of Glasgow microanalysis service. Variable-temperature, solid-state direct current (dc) magnetic susceptibility data down to 2.0 K were collected on a Quantum Design MPMS-XL SQUID magnetometer equipped with a 5 T DC magnet at the University of Glasgow. Polycrystalline samples were embedded in eicosane and diamagnetic corrections were applied to the observed paramagnetic susceptibilities using Pascal's constants. Powder XRD measurements were collected on freshly prepared samples of **1**, **2**, **1@Y** and **2@Y** on a PANalytical X'Pert Pro MPD diffractometer (λ ($CuK\alpha_1$) = 1.4505 Å) on a mounted bracket sample stage, at the University of Glasgow. Single Crystal X-Ray diffraction data were collected using a Bruker D8 VENTURE diffractometer equipped with a Photon II CMOS detector, with an Oxford Cryosystems N-Helix device mounted on an IμS 3.0 (dual Cu and Mo) microfocus sealed tube generator at the University of Glasgow.

Synthesis

Synthetic strategy applicable to **1-4***:*

Hexamethylphosphoramide (306 mg, 1.7 mmol) was added to 10 ml of hot THF. After 30 minutes, $DyCl_3 \cdot 6H_2O$ (113 mg, 0.3 mmol), was added to give a colourless solution. After stirring for 2 hours, the solution was evaporated to dryness and the precipitate formed was dissolved in a mixture of DCM/Toluene (1:1) and was left for slow evaporation. After ~ 3 days colourless single crystals of $[Dy(H_2O)_5(HMPA)_2]Cl_3 \cdot HMPA \cdot H_2O$ (**1**) were isolated. For $[Dy(H_2O)_5(HMPA)_2]I_3 \cdot 2HMPA$ (**2**), $[Y(H_2O)_5(HMPA)_2]Cl_3 \cdot HMPA \cdot H_2O$ (**3**) and $[Y(H_2O)_5(HMPA)_2]I_3 \cdot 2HMPA$ (**4**), exactly the same procedure was followed as in the case of **1**, with the use of DyI_3 (163 mg, 0.3 mmol), $YCl_3 \cdot 6H_2O$ (91 mg, 0.3 mmol) or YI_3 (141 mg, 0.3 mmol) respectively. Typical yields of compounds **1**-**4** are 30-35%.

Elemental Anal. calcd (found) for **1**$\cdot H_2O$: C 23.64 (23.48), H 7.27 (7.28), N 13.78 (13.45) %. **2**: C 21.35 (21.41), H 6.12 (6.10), N 12.45 (12.35) %. **3**: C 25.70 (25.71), H 7.91 (7.91), N 14.96 (14.99) %. **4**: C 22.58 (22.90), H 6.48 (6.44), N 13.17 (12.90) %.

Synthetic strategy applicable to **1@Y***:*

The same procedure was followed as in the case of **1** with the use of hexamethylphosphoramide (1026 mg, 5.7 mmol), $DyCl_3 \cdot 6H_2O$ (19 mg, 0.05 mmol) and $YCl_3 \cdot 6H_2O$ (288 mg, 0.95 mmol).

Elemental Anal. calcd (found) for **1@Y**$\cdot 1H_2O$: C 25.71 (25.72), H 7.91 (7.93), N 14.99 (14.53) %.

Synthetic strategy applicable to **2@Y***:*

The same procedure was followed as in the case of **2** with the use of hexamethylphosphoramide (1026 mg, 5.7 mmol), DyI_3 (27 mg, 0.05 mmol) and YI_3 (447 mg, 0.95 mmol).

Elemental Anal. calcd (found) for **2@Y**$\cdot 0.5H_2O$: C 22.58 (23.03), H 6.48 (7.12), N 13.17 (13.09) %.

Single-Crystal X-ray Diffraction

Selected details of the single crystal X-ray diffraction studies of **1-4** are provided below. More complete details are provided in the deposited CIFs (CCDC 1835322-1835325). In all cases one HMPA ligand shows some disorder, details of the disorder modelling are provided in the CIFs.

Data collection: *APEX3* Ver. 2016.9-0 (Bruker-AXS, 2016); cell refinement: *SAINT* v8.37A (Bruker, 2015); data reduction: *SAINT* v8.37A (Bruker, 2015); program(s) used to solve structure: SHELXT (Sheldrick, 2015); program(s) used to refine structure: SHELXL (Sheldrick, 2008); within Olex2 (Dolomanov *et al.*, 2009).[1,2,3]

Table S1. Crystallographic data for complexes **1** and **2**.

	1	**2**
Formula	$C_{18}H_{66}Cl_3DyN_9O_9P_3$	$C_{24}H_{82}DyI_3N_{12}O_9P_4$
M_W	914.55	1350.09
Crystal System	Monoclinic	Monoclinic
Space group	$P2_1/c$	Cc
a/Å	11.3237 (10)	14.0512 (7)
b/Å	38.167 (4)	19.1355 (10)
c/Å	19.4676 (18)	20.4829 (11)
α/°	90	90
β/°	101.025 (3)	101.075 (2)
γ/°	90	90
V/Å^3	8258.4 (13)	5404.8 (5)
Z	8	4
T/K	100	100
λ/Å	0.71073	0.71073
D_c/g cm^{-3}	1.471	1.659
μ(Mo-K$_\alpha$)/ mm^{-1}	2.17	3.26

Meas./indep.(R_{int}) refl.	97180 /18913 (0.033)	24453/11023 (0.029)
Obs. refl. [$I>2\sigma(I)$]	17718	10586
$wR(F^2)$	0.054	0.054
$R[F^2 > 2s(F^2)]$	0.025	0.024
S	1.15	0.98
$\Delta\rho_{max,min}$/ eÅ^{-3}	0.90, -1.35	1.17, -0.66

Table S2. Crystallographic data for complexes **3** and **4**.

	3	**4**
Formula	$C_{18}H_{66}Cl_3YN_9O_9P_3$	$C_{24}H_{82}YI_3N_{12}O_9P_4$
M_W	840.96	1276.50
Crystal System	Monoclinic	Monoclinic
Space group	$P2_1/c$	Cc
a/Å	11.4154 (7)	14.0960 (8)
b/Å	38.613 (3)	19.1099 (13)
c/Å	19.9862 (13)	20.5439 (13)
α/°	90	90
β/°	101.936 (3)°	101.091 (2)
γ/°	90	90
V/Å^3	8619.2 (10)	5430.6 (6)
Z	8	4
T/K	298	295
λ/Å	0.71073	0.71073 Å
D_c/g cm^{-3}	1.296	1.561

μ(Mo-K_α)/ mm^{-1}	1.70	2.95
Meas./indep.(R_{int}) refl.	94898/19662(0.054)	52651/12236(0.086)
Obs. refl. [$I>2\sigma(I)$]	13854	10497
$wR(F^2)$	0.123	0.056
$R[F^2 > 2s(F^2)]$	0.047	0.029
S	1.02	1.04
$\Delta\rho_{max,min}$/ $eÅ^{-3}$	0.70, -0.49	0.57, −0.87

Table S2. Selected bond distances and angles for complex **1** (Å, º).

Dy1—O3	2.2171 (14)	Dy1—O8W	2.3600 (16)
Dy1—O4	2.2211 (14)	Dy1—O9W	2.3433 (16)
Dy1—O6W	2.3474 (16)	Dy1—O10W	2.3576 (16)
Dy1—O7W	2.3377 (16)		
O3—Dy1—O4	175.58 (6)	O6W—Dy1—O10W	71.85 (6)
O3—Dy1—O6W	93.38 (6)	O7W—Dy1—O6W	71.85 (6)
O3—Dy1—O7W	90.13 (6)	O7W—Dy1—O8W	72.63 (6)
O3—Dy1—O8W	89.73 (6)	O7W—Dy1—O9W	144.53 (7)
O3—Dy1—O9W	87.50 (6)	O7W—Dy1—O10W	143.21 (6)
O3—Dy1—O10W	86.19 (6)	O9W—Dy1—O6W	143.62 (6)
O4—Dy1—O6W	89.78 (6)	O9W—Dy1—O8W	71.97 (6)
O4—Dy1—O7W	93.80 (6)	O9W—Dy1—O10W	71.93 (6)
O4—Dy1—O8W	89.50 (6)	O10W—Dy1—O8W	143.80 (6)
O4—Dy1—O9W	88.12 (6)	O4—Dy1—O10W	91.86 (6)

O6W—Dy1—O8W	144.34 (6)		
Dy2—O1	2.2282 (15)	Dy2—O2W	2.3587 (17)
Dy2—O1W	2.3586 (16)	Dy2—O3W	2.3465 (17)
Dy2—O2	2.2096 (15)	Dy2—O4W	2.3386 (17)
Dy2—O5W	2.3365 (16)		
O1—Dy2—O1W	90.67 (6)	O2—Dy2—O3W	87.38 (7)
O1—Dy2—O2W	86.05 (6)	O2—Dy2—O4W	91.00 (6)
O1—Dy2—O3W	95.79 (6)	O2—Dy2—O5W	90.12 (6)
O1—Dy2—O4W	89.12 (6)	O3W—Dy2—O1W	143.43 (7)
O1—Dy2—O5W	86.78 (6)	O3W—Dy2—O2W	72.05 (7)
O1W—Dy2—O2W	72.56 (7)	O4W—Dy2—O1W	143.89 (6)
O2—Dy2—O1	176.71 (6)	O4W—Dy2—O2W	143.35 (7)
O2—Dy2—O1W	87.29 (6)	O4W—Dy2—O3W	72.35 (7)
O2—Dy2—O2W	95.79 (6)	O5W—Dy2—O1W	71.41 (6)
O5W—Dy2—O2W	143.12 (7)	O5W—Dy2—O4W	72.53 (6)
O5W—Dy2—O3W	144.73 (7)		

Table S3. Selected bond distances and angles for complex **2** (Å, º).

Dy1—O1	2.202 (4)	Dy1—O3W	2.343 (4)
Dy1—O2	2.208 (4)	Dy1—O4W	2.364 (4)
Dy1—O1W	2.375 (4)	Dy1—O5W	2.359 (4)
Dy1—O2W	2.357 (4)		
O1—Dy1—O2	177.95 (16)	O2W—Dy1—O1W	73.00 (14)

O1—Dy1—O1W	89.28 (14)	O2W—Dy1—O4W	142.07 (14)
O1—Dy1—O2W	89.41 (16)	O2W—Dy1—O5W	146.17 (13)
O1—Dy1—O3W	89.18 (15)	O3W—Dy1—O1W	144.26 (14)
O1—Dy1—O4W	92.92 (16)	O3W—Dy1—O2W	71.28 (14)
O1—Dy1—O5W	90.45 (16)	O3W—Dy1—O4W	70.91 (14)
O2—Dy1—O1W	89.15 (14)	O3W—Dy1—O5W	142.55 (14)
O2—Dy1—O2W	88.88 (17)	O4W—Dy1—O1W	144.82 (14)
O2—Dy1—O3W	91.34 (15)	O5W—Dy1—O1W	73.18 (14)
O2—Dy1—O4W	89.12 (16)	O5W—Dy1—O4W	71.71 (14)
O2—Dy1—O5W	90.35 (16)		

Table S4. Shape measures of complex **1**. The lowest CShMs value, is highlighted.[4]

	Dy1 (1a)	**Symmetry**	**Ideal polyhedron**
HP-7	34.323	D7h	Heptagon
HPY-7	25.016	C6v	Hexagonal pyramid
PBPY-7	**0.154**	**D5h**	**Pentagonal bipyramid**
COC-7	7.242	C3v	Capped octahedron
CTPR-7	5.574	C2v	Capped trigonal prism
JPBPY-7	2.809	D5h	Johnson pentagonal bipyramid J13
JETPY-7	24.125	C3v	Johnson elongated triangular pyramid J7

	Dy2 (1b)	**Symmetry**	**Ideal polyhedron**
HP-7	34.232	D7h	Heptagon
HPY-7	25.430	C6v	Hexagonal pyramid
PBPY-7	**0.284**	**D5h**	**Pentagonal bipyramid**
COC-7	6.547	C3v	Capped octahedron
CTPR-7	4.797	C2v	Capped trigonal prism
JPBPY-7	2.964	D5h	Johnson pentagonal bipyramid J13
JETPY-7	23.336	C3v	Johnson elongated triangular pyramid J7

Table S5. Shape measures of complex **2**.

	Dy	**Symmetry**	**Ideal polyhedron**
HP-7	34.315	D7h	Heptagon
HPY-7	25.127	C6v	Hexagonal pyramid
PBPY-7	**0.131**	**D5h**	**Pentagonal bipyramid**
COC-7	7.780	C3v	Capped octahedron
CTPR-7	5.911	C2v	Capped trigonal prism
JPBPY-7	2.617	D5h	Johnson pentagonal bipyramid J13
JETPY-7	24.592	C3v	Johnson elongated triangular pyramid J7

Table S6. CASSCF+RASSI-SO computed relative energies (*in* cm^{-1}) of eight low lying Kramer's Doublets along with g tensors and deviations from the principal magnetization axes with respect to first KD for complexes **1** (Unit **1a** *top* and unit **1b** *middle*) and **2** (*bottom*). Note: Complex **1** has two crystallographic units (**1a** and **1b**) and calculations have been performed on both units.

E / cm^{-1}	**g_{xx}**	**g_{yy}**	**g_{zz}**	**Angle / °**
0.00	0.000	0.000	19.988	
298.50	0.008	0.011	17.126	0.8
409.51	0.685	2.474	17.710	89.4
468.87	8.380	6.312	3.821	3.6
498.15	0.221	0.380	13.131	4.5
532.20	0.455	2.593	8.066	24.4
595.18	8.836	6.022	2.126	111.0
604.83	10.917	7.319	1.527	57.6

E / cm^{-1}	**g_{xx}**	**g_{yy}**	**g_{zz}**	**Angle / °**
0.00	0.000	0.000	19.959	
294.37	0.011	0.015	17.061	1.6
405.67	0.581	1.856	18.143	91.8
469.85	3.754	6.002	8.851	108.4
495.13	1.464	1.948	11.357	9.3
539.49	0.642	2.177	8.478	20.4
593.13	0.611	2.237	15.222	49.3
613.14	0.235	0.878	17.241	54.1

E / cm^{-1}	g_{xx}	g_{yy}	g_{zz}	Angle / °
0.00	0.000	0.000	19.971	
307.76	0.023	0.024	17.116	1.7
444.69	11.777	9.309	1.320	0.8
488.88	0.858	1.561	4.192	11.4
519.43	0.014	0.437	13.556	3.8
563.86	2.008	2.679	7.436	14.2
616.90	1.362	1.777	11.961	30.9
638.69	0.566	0.879	15.136	45.7

Table S7 *Ab initio* SINGLE_ANISO computed crystal field parameters for complexes **1** and **2**. Complex **2** has larger crystal field than **1**. Note: Complex **1** has two crystallographic units (**1a** and **1b**) and calculations have been performed on both units.

Here, k - the rank of the ITO, = 2, 4, 6, 8, 10, 12.

q - the component of the ITO, = -k, -k+1, ... 0, 1, ... k;

K_m^n are proportionality coefficients between the ESO and operators. The non-axial term (B_k^q, where q ≠ 0 and k = 2, 4, and 6) to the axial term (B_k^q, where q = 0 and k = 2, 4, and 6) ratio should be smaller for lesser operational QTM and larger U_{cal} value.

k	q	K_m^n	Complexes B_k^q		
			1a	**1b**	**2**
2	-2	1.5	-0.27	0.76	0.00
2	-1	6.0	-0.26	0.02	0.51
2	0	1.0	-2.43	-2.24	-2.58
2	1	6.0	-0.06	-0.39	0.24
2	2	1.5	0.65	0.30	0.08

Table S8 *Ab initio* SINGLE_ANISO computed crystal field parameters for different models created by defragmentation of complexes **1b** and **2** (**1b** top and **2** bottom). For more details, see Fig. S28 and Fig. S29. Note: Complex **1** has two crystallographic units (**1a** and **1b**) and the anisotropy properties for both units of complex **1** are expected to be practically identical, as seen from magnetic blockade diagrams (Figure S29), so we have performed defragmentation only on unit **1b**. A smaller ratio of the non-axial term (B_k^q, where q ≠ 0 and k = 2, 4, and 6) to the axial term (B_k^q, where q = 0 and k = 2, 4, and 6) is needed for lesser operational QTM. Removal of transverse anions/ligand-component cause lowering of the non-axial term (B_k^q, where q ≠ 0 and k = 2, 4, and 6) to the axial term (B_k^q, where q = 0 and k = 2, 4, and 6) ratio and decrease operational QTM. The smallest ratio is found for the two coordinated linear models (**1b**-(1-12) and **2**-(1-10)), resulting in a very large U_{cal} value of ~3100 K.

Complex **1**															
k	q	B_k^q													
		1b	**1b**-1	**1b**-(1-2)	**1b**-(1-3)	**1b**-(1-4)	**1b**-(1-5)	**1b**-(1-6)	**1b**-(1-7)	**1b**-(1-8)	**1b**-(1-9)	**1b**-(1-10)	**1b**-(1-11)	**1b**-(1-12)	**1a**
2	-2	0.76	0.70	0.72	0.86	0.15	-0.63	-0.05	0.32	0.27	-0.04	2.90	0.02	0.11	-0.27
2	-1	0.02	0.16	0.15	0.20	0.30	0.12	0.14	0.84	0.05	0.98	-0.34	-0.10	0.25	-0.26
2	0	-2.44	-2.72	-2.67	-3.20	-3.68	-4.75	-5.51	-6.90	-8.53	-10.04	-11.74	-13.44	-6.49	-2.43
2	1	-0.39	-0.35	-0.36	-0.37	-0.38	-0.25	0.07	-1.10	0.50	0.43	0.14	0.04	-0.05	-0.06
2	2	0.30	0.79	0.68	1.01	0.49	0.58	-0.26	-0.19	0.16	11.37	-4.31	0.18	0.00	0.65

Complex **2**													
k	q	B_k^q											
		2	**2**-1	**2**-(1-2)	**2**-(1-3)	**2**-(1-4)	**2**-(1-5)	**2**-(1-6)	**2**-(1-7)	**2**-(1-8)	**2**-(1-9)	**2**-(1-10)	**2**-(1-11)
2	-2	0.00	-0.02	0.03	0.14	0.44	-0.02	0.32	0.27	-0.04	2.90	0.02	0.11
2	-1	0.51	0.37	0.10	0.35	0.34	0.17	0.84	0.05	0.98	-0.34	-0.10	0.25
2	0	-2.58	-3.09	-3.69	-4.34	-5.01	-5.68	-6.90	-8.53	-10.04	-11.74	-13.44	-6.49
2	1	0.24	-0.33	-0.57	0.29	-0.30	0.54	-1.10	0.50	0.43	0.14	0.04	-0.05
2	2	0.08	0.44	-0.54	0.20	-0.43	0.08	-0.19	0.16	11.37	-4.31	0.18	0.00

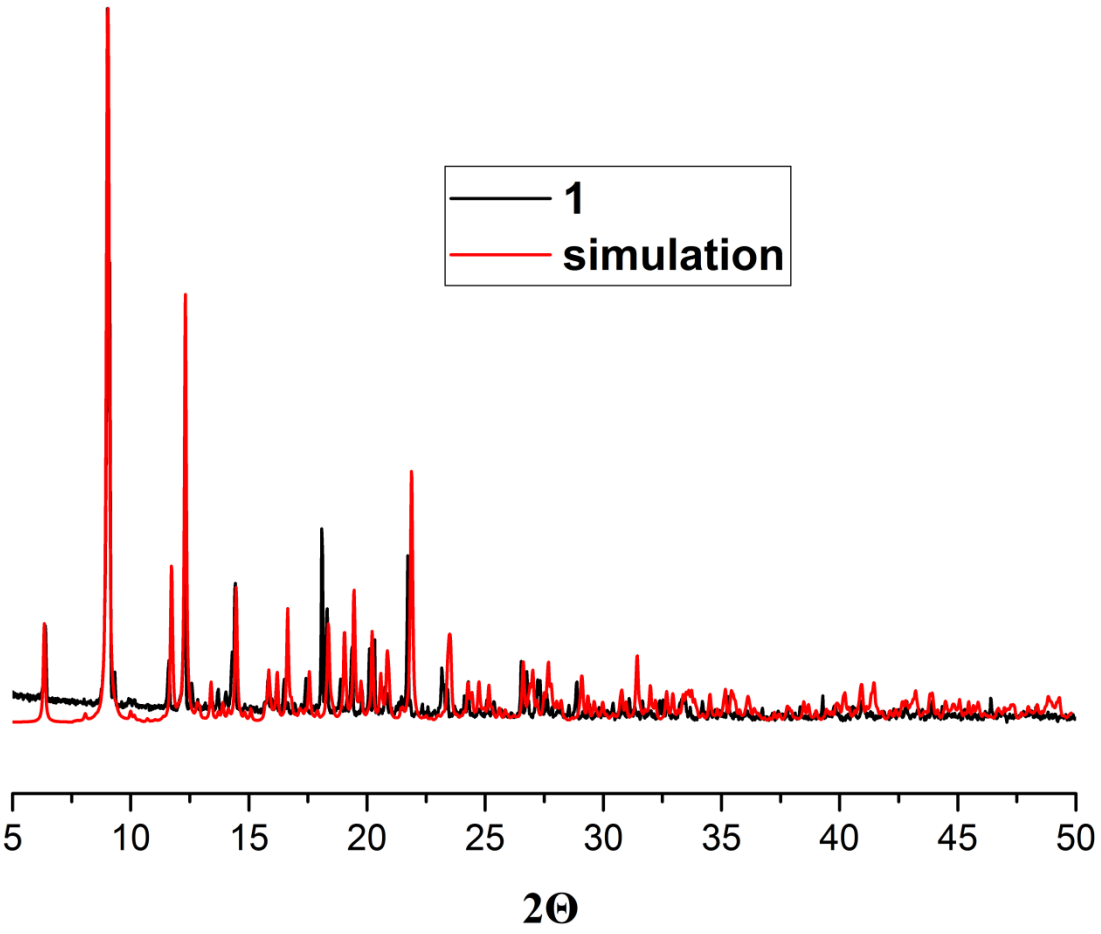

Fig. S1 The powder X-ray diffraction pattern of **1.** The red line represents the simulated powder X-ray diffraction pattern generated from single-crystal data collected at 100 K, and the black line represents the experimental data measured at ambient temperature.

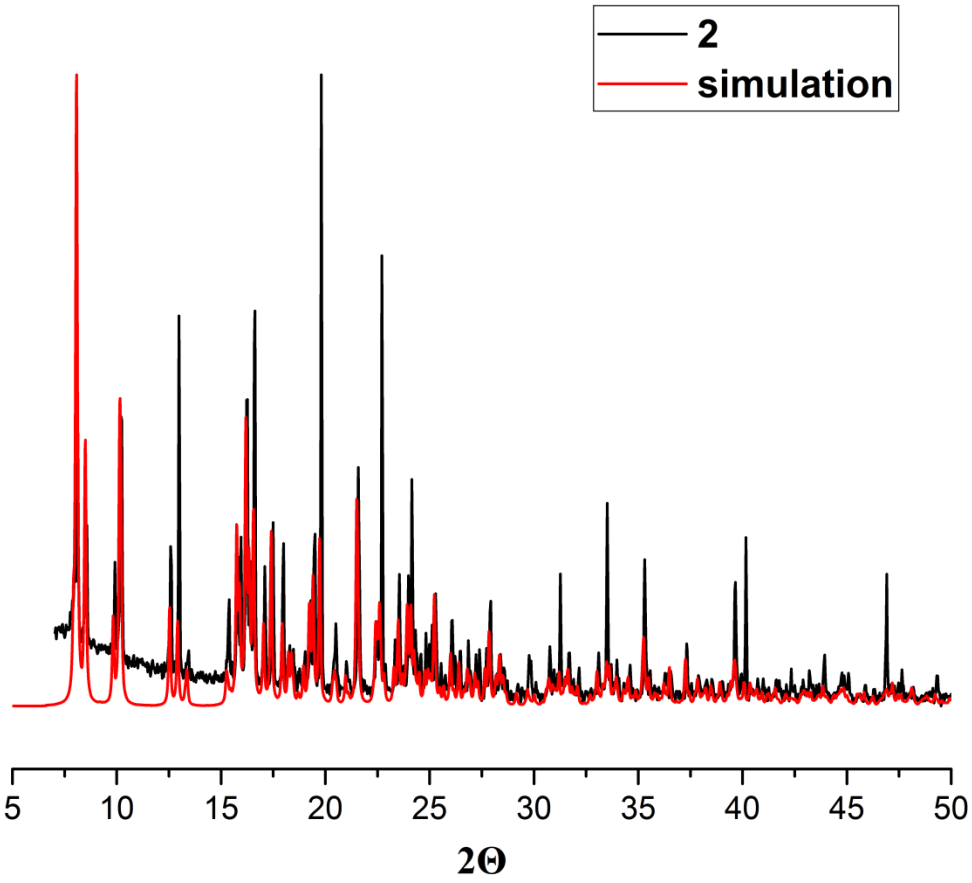

Fig. S2 The powder X-ray diffraction pattern of **2.** The red line represents the simulated powder X-ray diffraction pattern generated from single-crystal data collected at 100 K, and the black line represents the experimental data measured at ambient temperature.

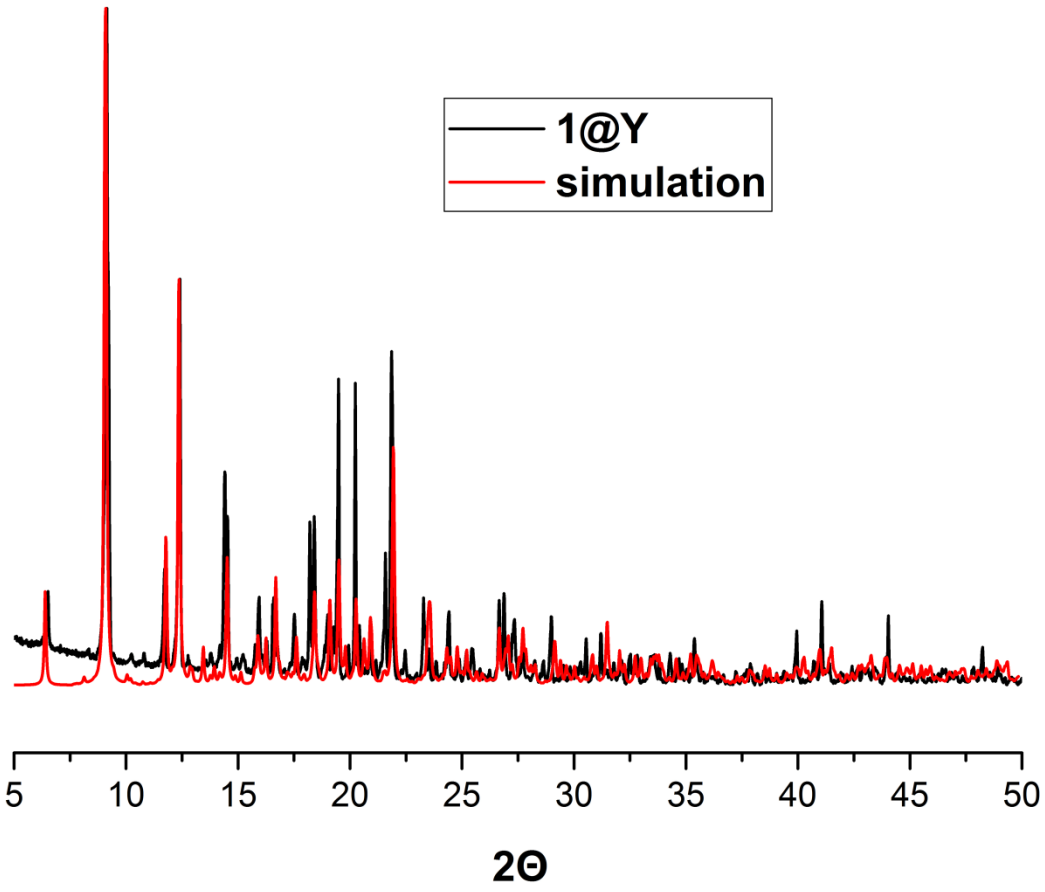

Fig. S3 The experimental powder X-ray diffraction pattern of **1@Y.** The red line represents the simulated powder X-ray diffraction pattern of **1** generated from single-crystal data collected at 100 K, and the black line represents the experimental data measured at ambient temperature.

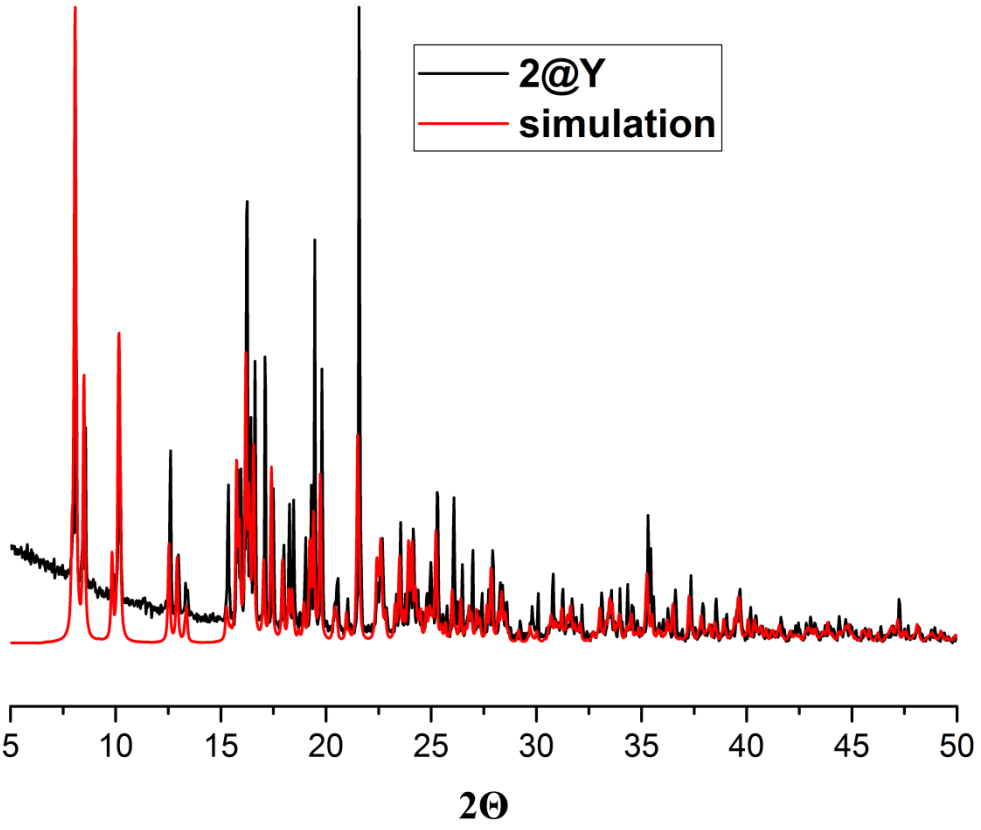

Fig. S4 The experimental powder X-ray diffraction pattern of **2@Y.** The red line represents the simulated powder X-ray diffraction pattern of **2** generated from single-crystal data collected at 100 K, and the black line represents the experimental data measured at ambient temperature.

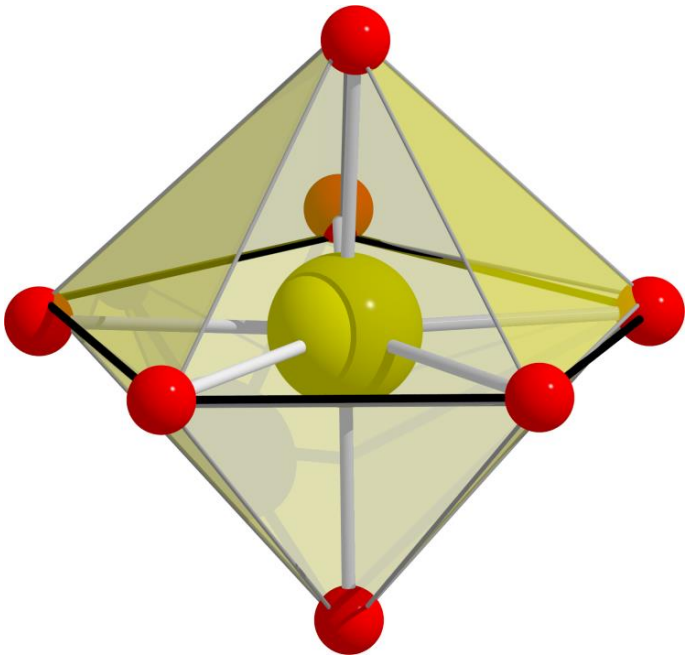

Fig. S5 Comparison of the calculated (with SHAPE[4]) and experimental pentagonal bipyramidal coordination sphere for Dy(III) ions in complexes **1** and **2**.

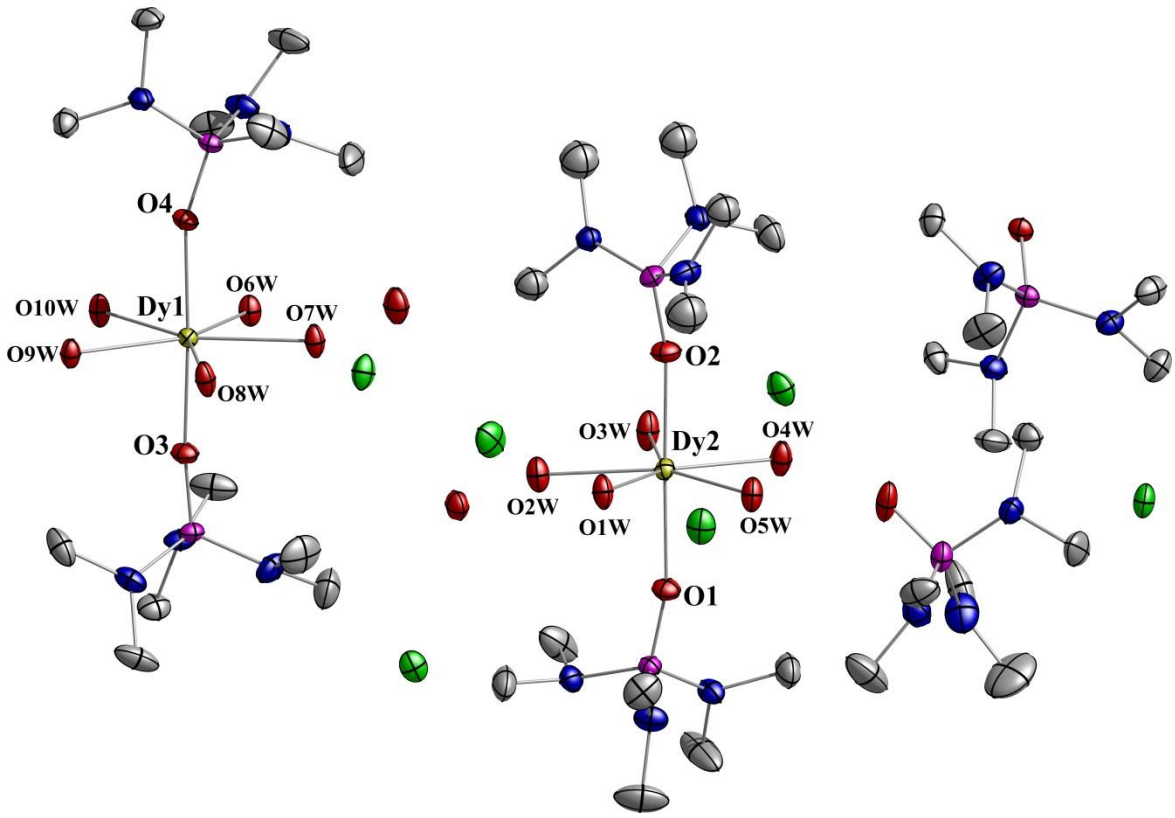

Fig. S6 The asymmetric unit of **1**. Dy, gold; O, red; N, blue, P, pink; Cl, green. The displacement ellipsoids are drawn at 50% probability level. Hydrogen atoms and disorder components are omitted for clarity.

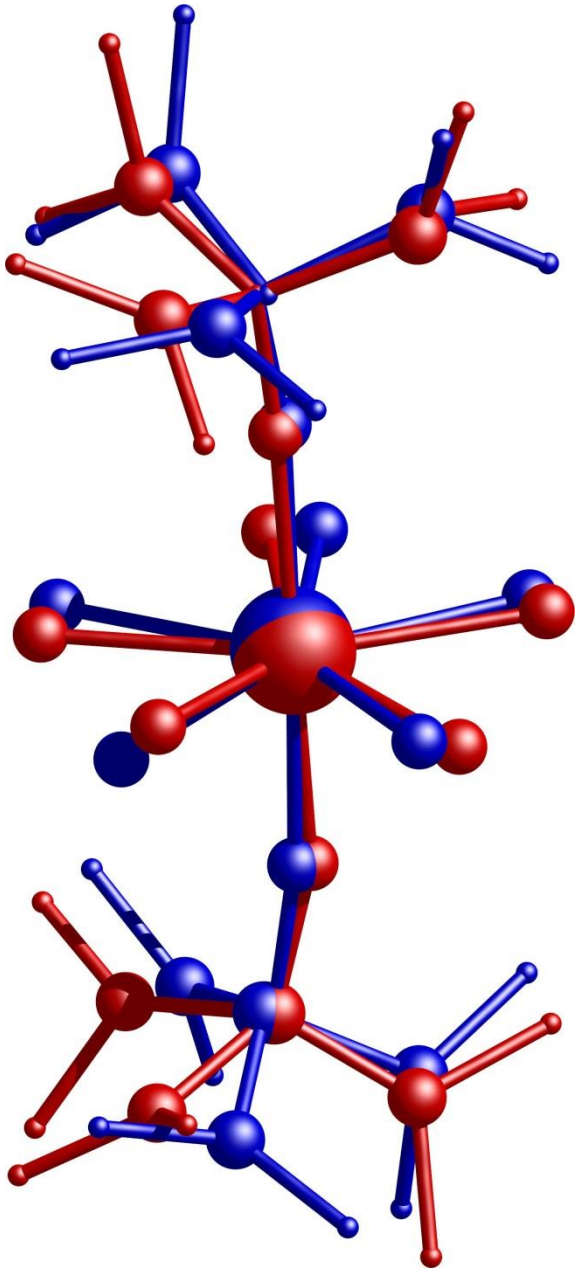

Fig. S7 Overlay of the two Dy molecules present in the asymmetric unit of complex **1** (1a, red; 1b, blue). Hydrogen atom, disorder components, counter ions, co-crystallised solvent molecules and co-crystallised HMPA ligands are omitted for clarity.

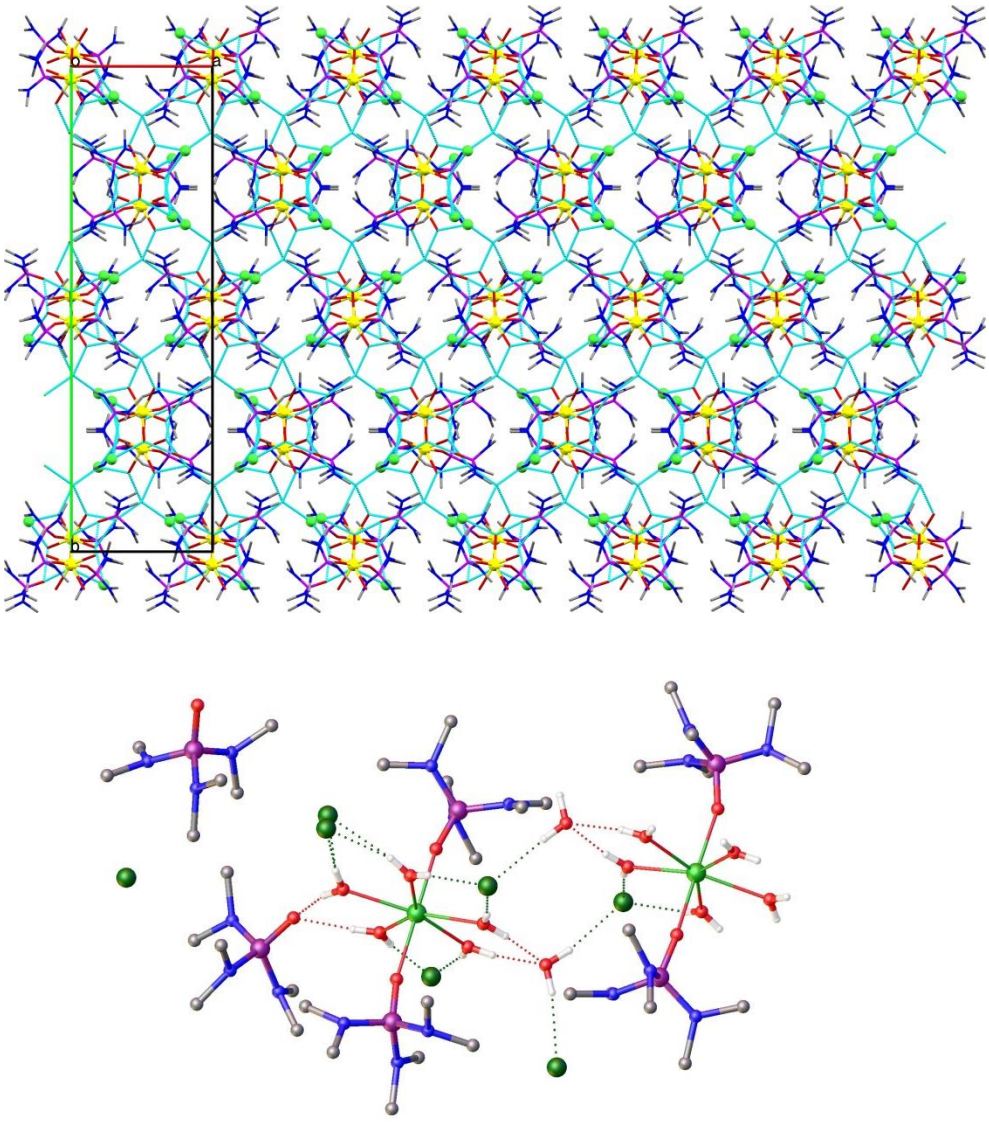

Fig. S8 (Top) Crystal packing of **1** highlighting the extensive hydrogen bonding between the molecules (indicated in light blue). View shown is looking down the *c*-axis. Dy, yellow; P, orange; Cl, green; O, red; C, gray; N, blue. Hydrogen atoms are omitted for clarity. (Bottom) Illustrating the hydrogen bonding between the molecules in the asymmetric unit. All hydrogens except water H and the minor disorder components were omitted for clarity. Dy, green; P, violet; Cl, dark green; O, red; C, gray; N, blue.

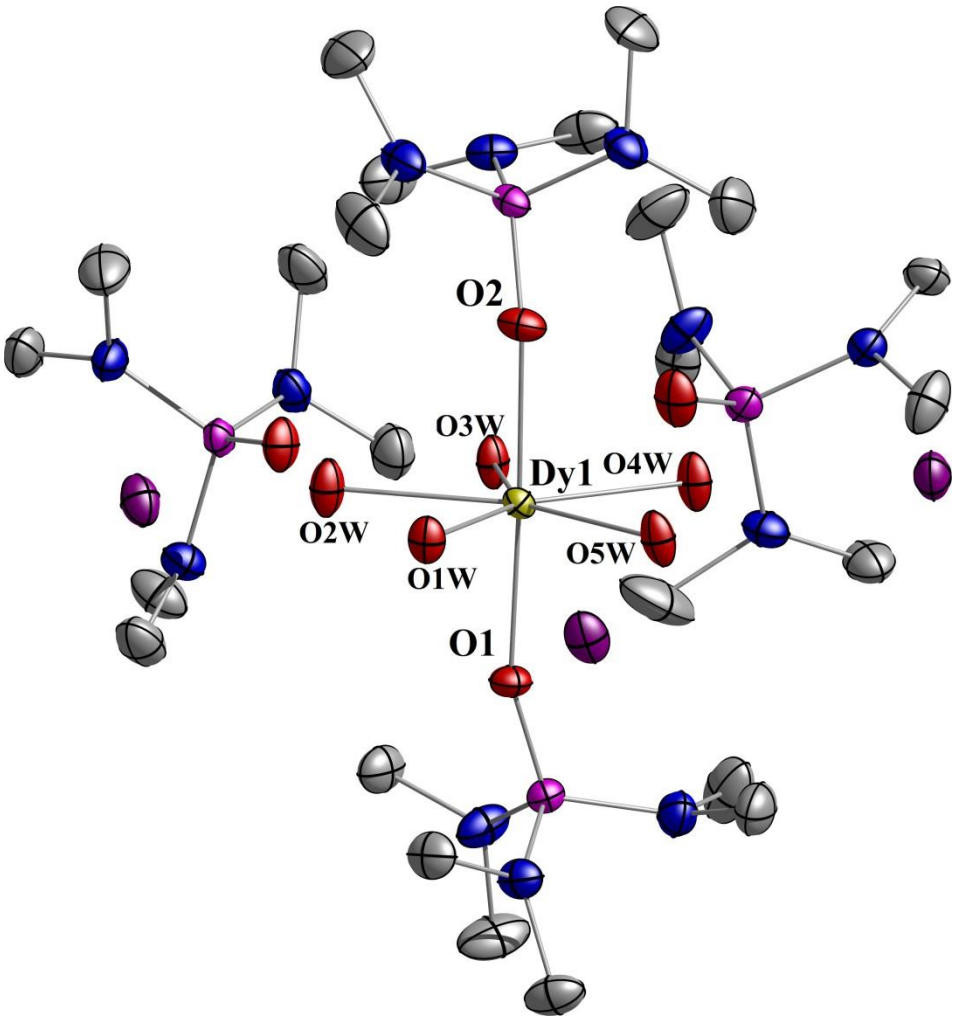

Fig. S9 The structure of **2.** Dy, gold; O, red; N, blue, P, pink; I, violet. The displacement ellipsoids are drawn at 50% probability level. Hydrogen atoms and disorder components are omitted for clarity.

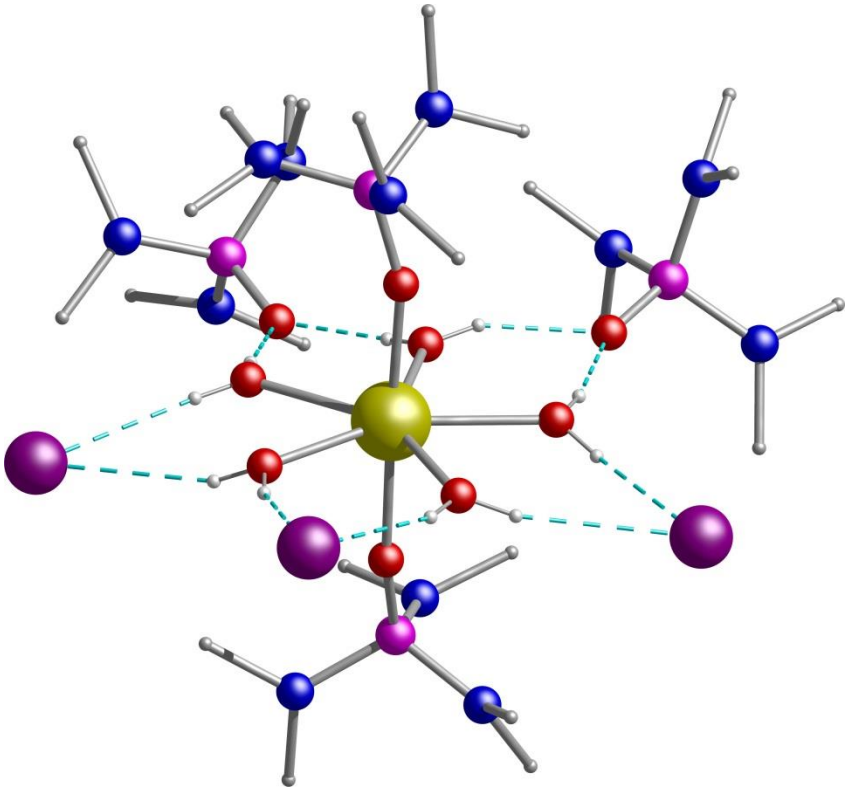

Fig. S10 Hydrogen bonding in **2**. Dy, yellow; P, pink; I, violet; O, red; C, gray; N, blue. Hydrogen atoms are omitted for clarity except the H atoms of the equatorial water ligands.

Magnetic Properties

Dc magnetic susceptibility measurement and magnetization for complex 1

For **1** the dc magnetic susceptibility measurements were performed in 290-2 K temperature range under an applied magnetic field of 0.1 T plotted as $\chi_M T$ vs. T in Fig. S10, with the isothermal magnetisation (*M* vs *H*) shown in Fig. S10 (inset). The room temperature $\chi_M T$ value of 14.12 cm^3 K mol^{-1} is in agreement with the theoretical value of 14.17 cm^3 K mol^{-1} expected for a mononuclear Dy (III) ion ($^6H_{15/2}$, S= 5/2, L = 5, g = 4/3). Upon cooling, the $\chi_M T$ value of complex **1** gradually decreases to 11.95 cm^3 K mol^{-1} at 6 K before rapidly dropping to the minimum value of 4.81 cm^3 K mol^{-1} at 2 K.

Dc magnetic susceptibility measurement for complex 2

For **2** the $\chi_M T$ value of 14.13 cm^3 K mol^{-1} at 290 K is close to the theoretical value of 14.17 cm^3 K mol^{-1} calculated for one Dy(III) ion (Fig. S11). Upon cooling the temperature, a relatively imperceptible decrease of the $\chi_M T$ is observed until 7 K following a more rapid decrease, reaching the value of 4.28 cm^3 K mol^{-1} at 2 K.

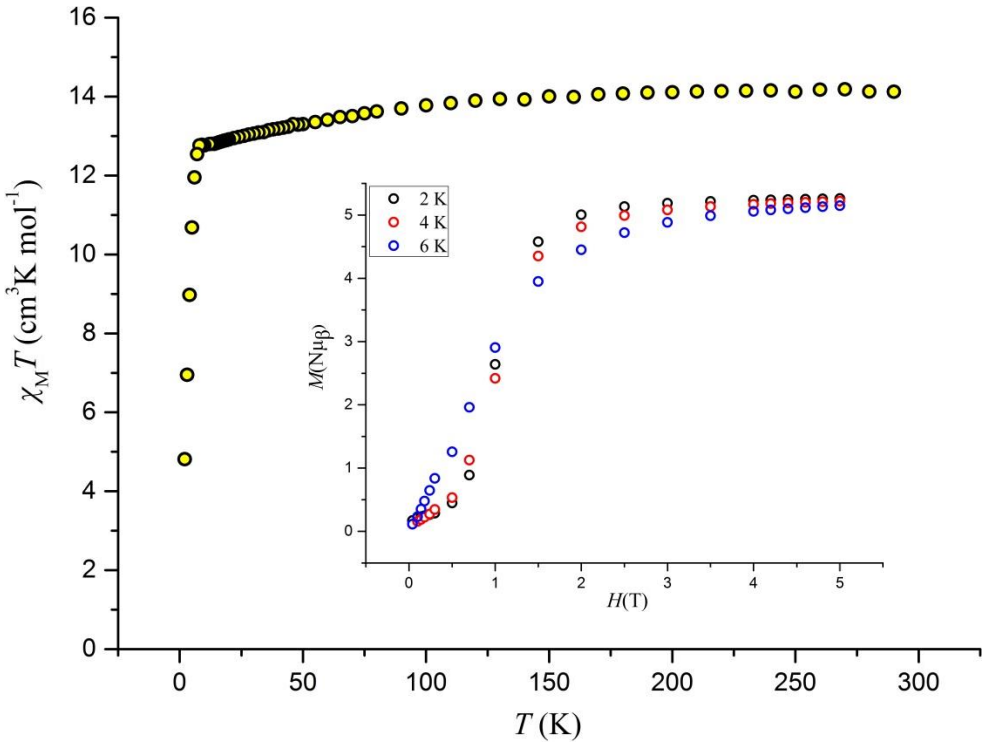

Fig. S11 $\chi_M T$ vs. T data for **1** in a field of 1000 Oe from 290 – 2 K. Inset: Magnetisation vs. Field plot at temperatures 2, 4 and 6 K for **1**.

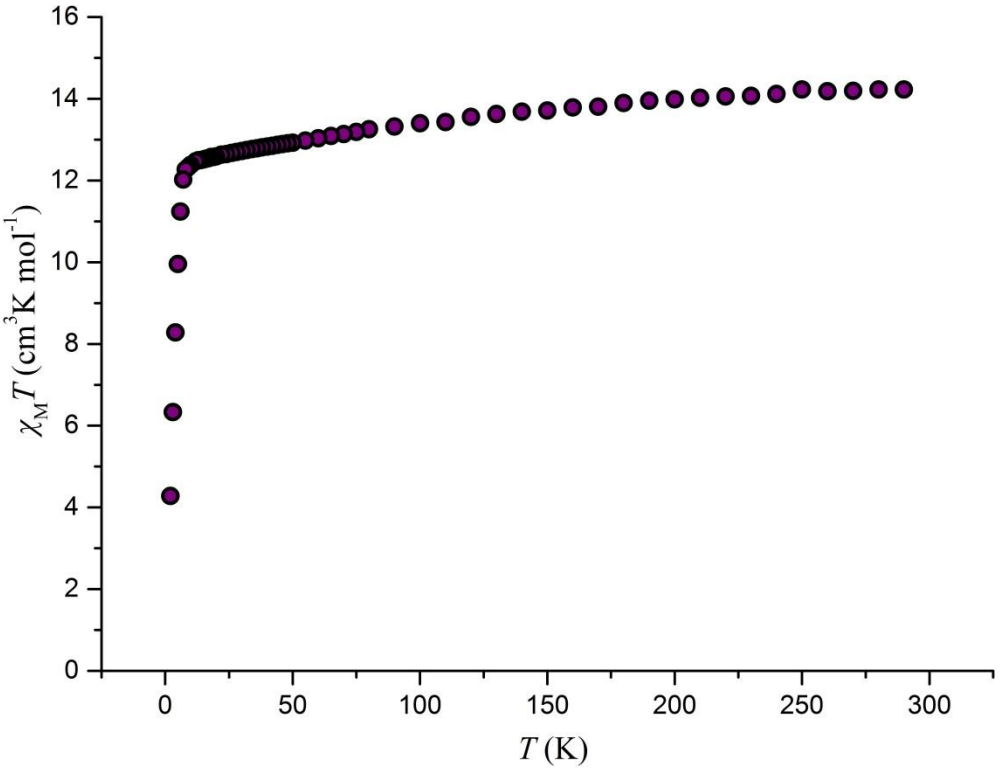

Fig. S12 $\chi_M T$ vs. T data for **2** in a field of 1000 Oe from 290 – 2 K.

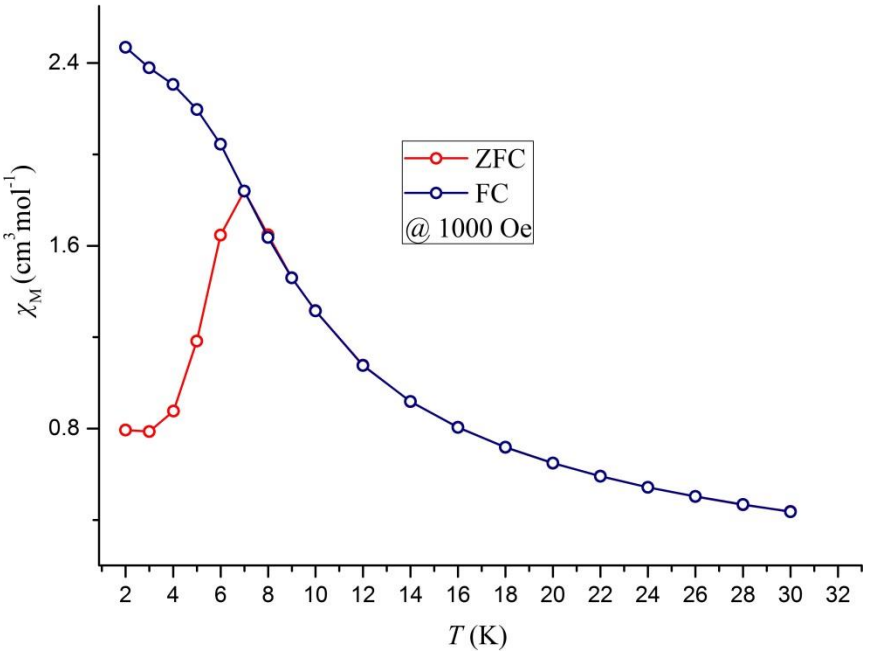

Fig. S13 The Field cooled (FC) and Zero-Field cooled (ZFC) magnetic susceptibility of **1** at 1000 Oe.

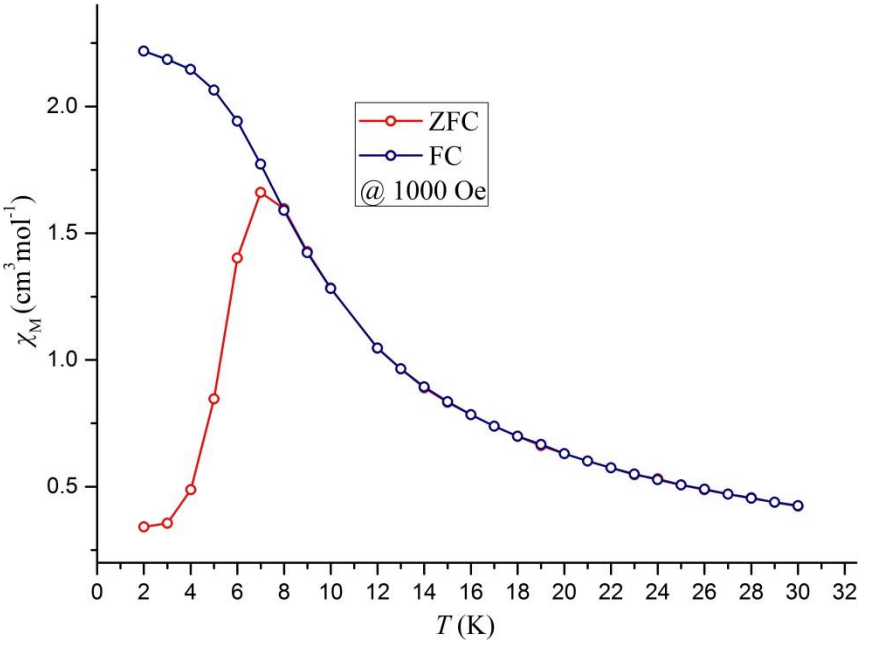

Fig. S14 The Field cooled (FC) and Zero-Field cooled (ZFC) magnetic susceptibility of **2** at 1000 Oe.

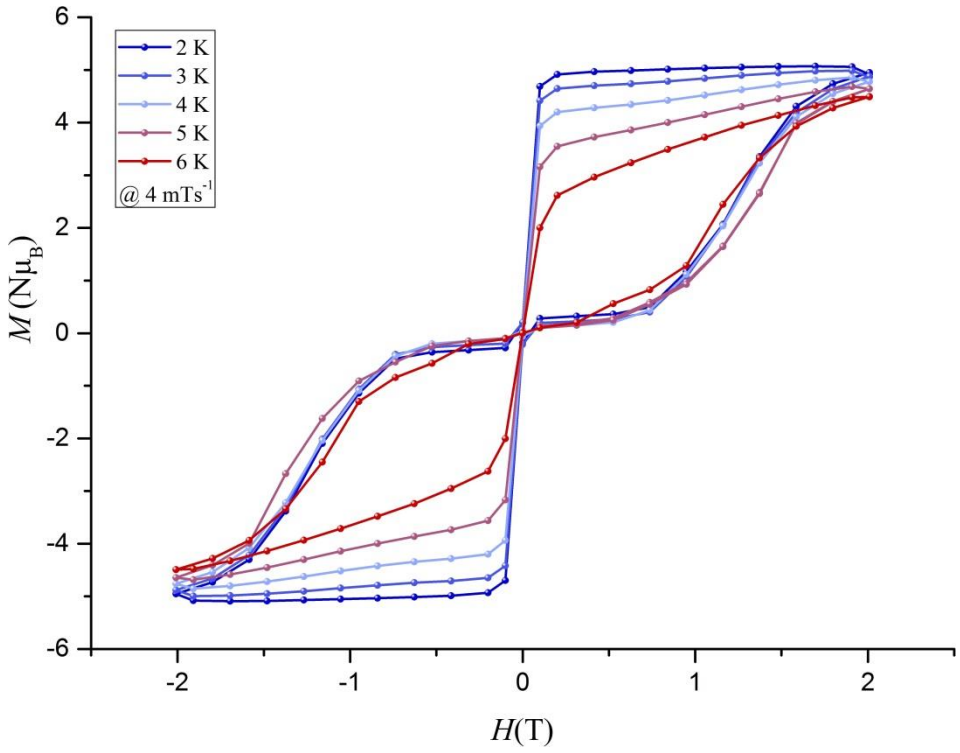

Fig. S15 Magnetic hysteresis measurements for **1** at 2-6 K with an average sweep rate of 4 mTs^{-1}.

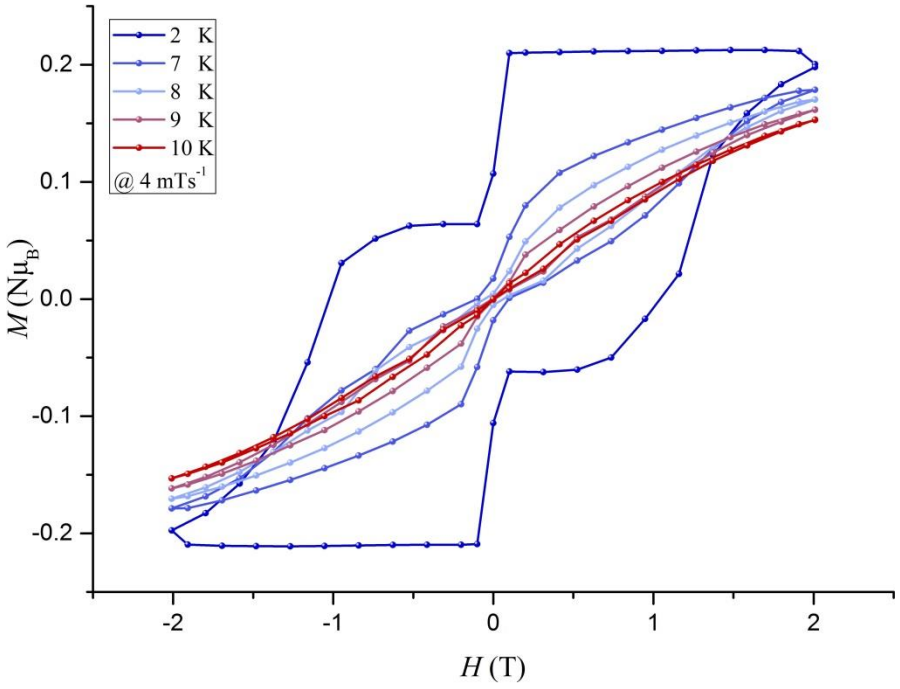

Fig. S16 Magnetic hysteresis measurements for **1@Y** at 2-10 K with an average sweep rate of 4 mTs^{-1}.

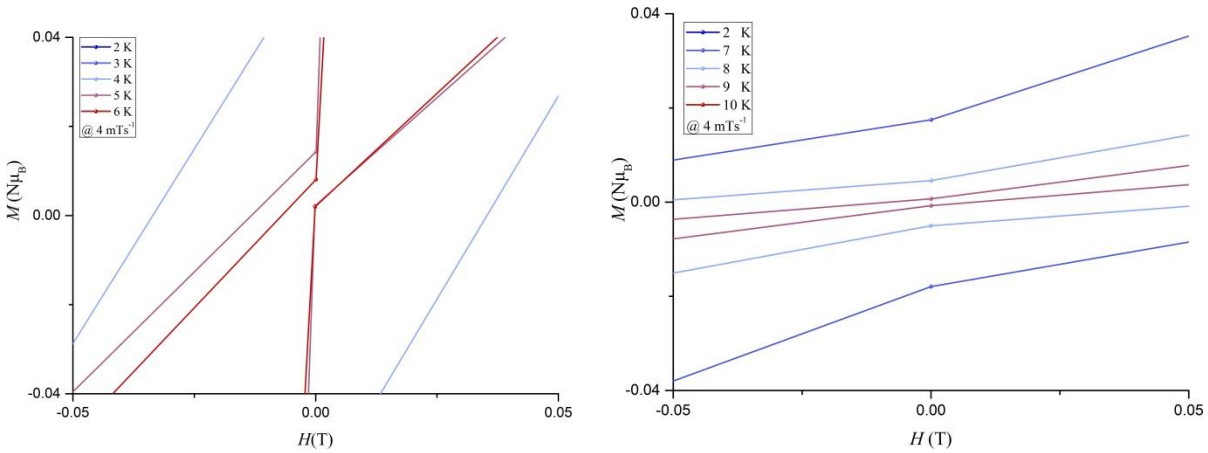

Fig. S17 (Left) Magnetic hysteresis measurements for **1** remaining open until 6 K**.** (Right) Magnetic hysteresis measurements for **1@Y** which remains open until 9 K.

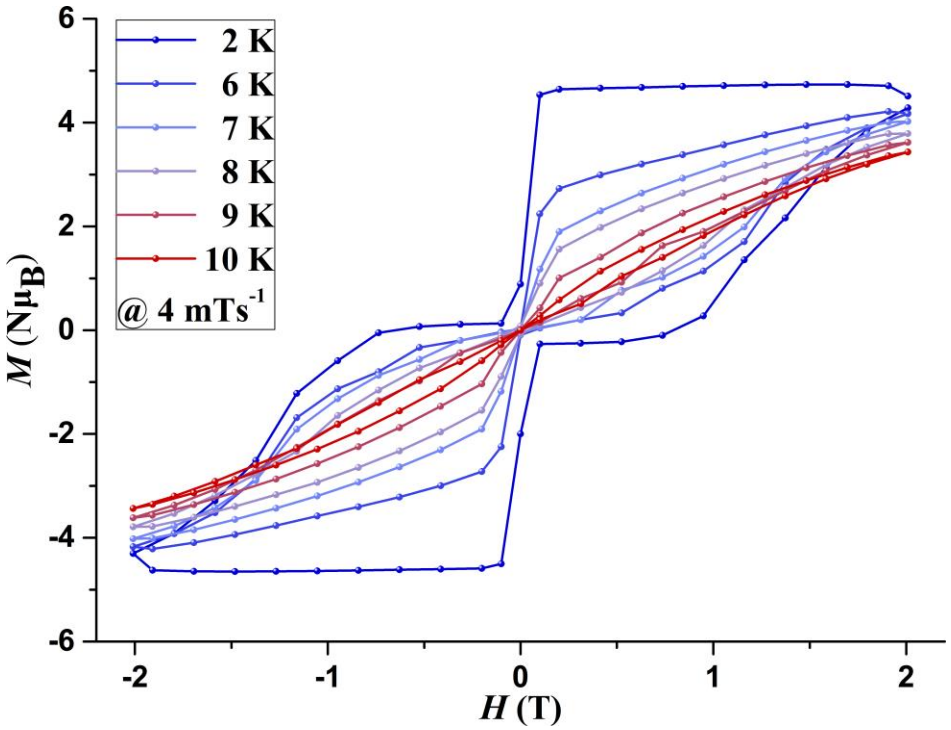

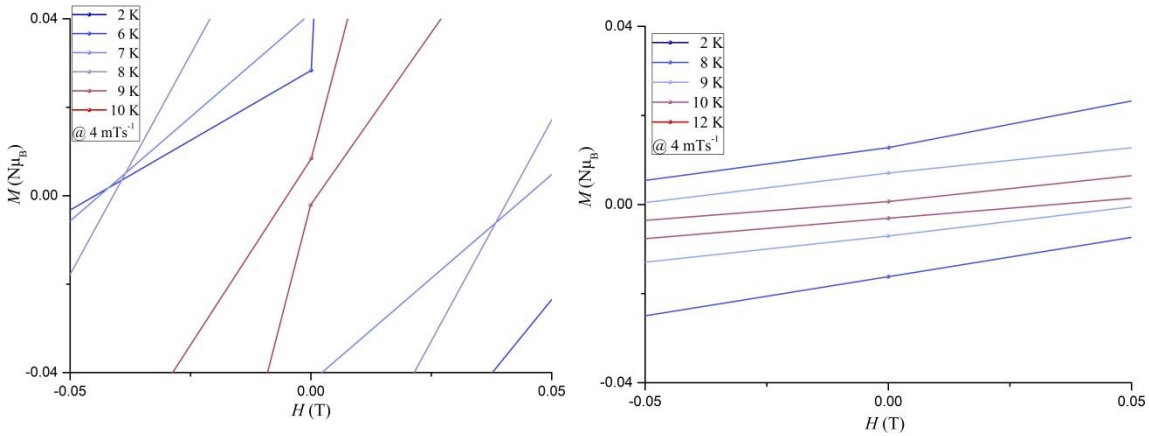

Fig. S18 (Top) Magnetic hysteresis measurements for **2**. (Bottom left) Magnetic hysteresis measurements for **2** remaining open until 9 K**.** (Bottom right) Magnetic hysteresis measurements for **2@Y** which remains open until 10 K.

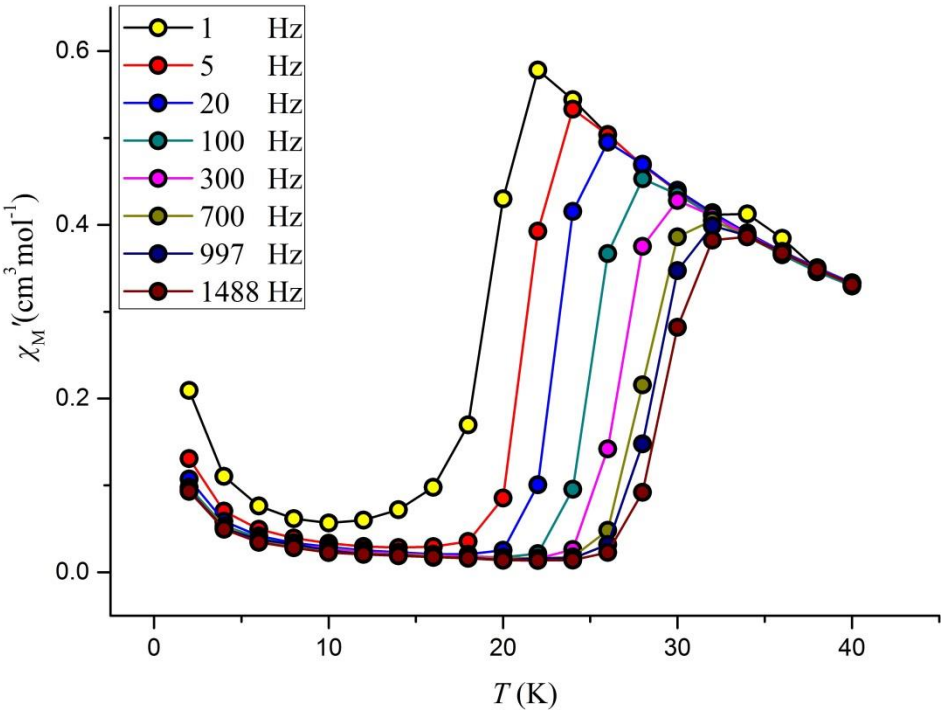

Fig. S19 Temperature dependence of the in-phase, χ'_M, product in zero dc field for **1** with ac frequencies of 1−1488 Hz.

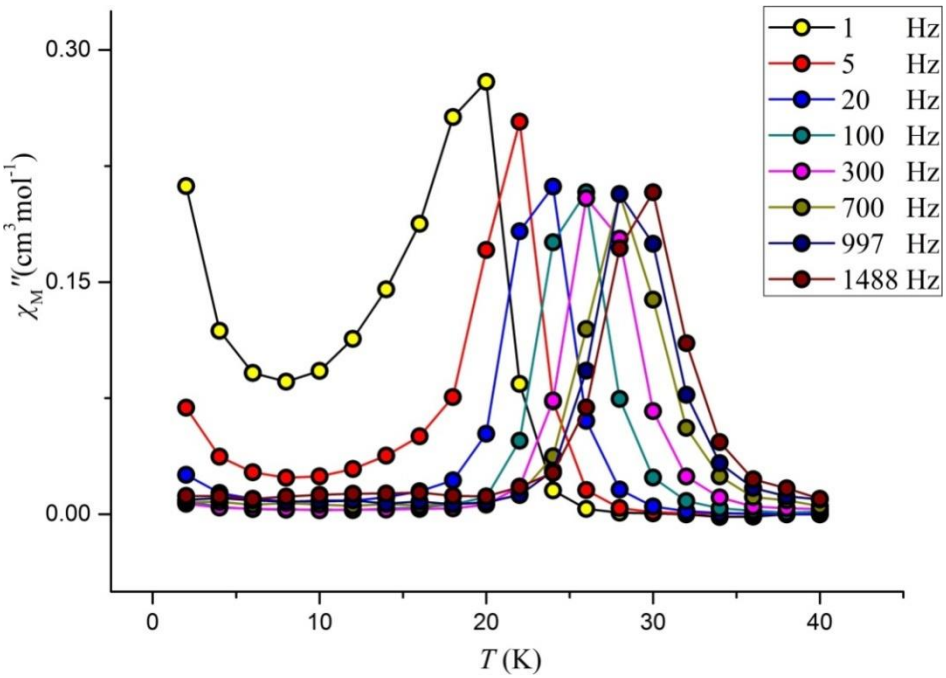

Fig. S20 Temperature dependence of the out-of-phase, χ''_M, product in zero dc field for **1** with ac frequencies of 1−1488 Hz.

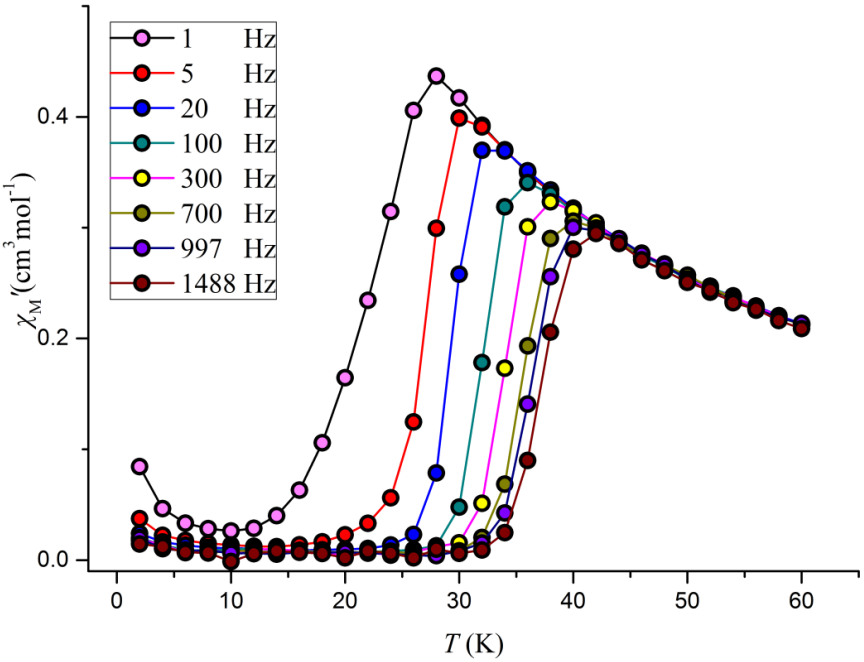

Fig. S21 Temperature dependence of the in-phase, χ'_M, product in zero dc field for **2** with ac frequencies of 1−1488 Hz.

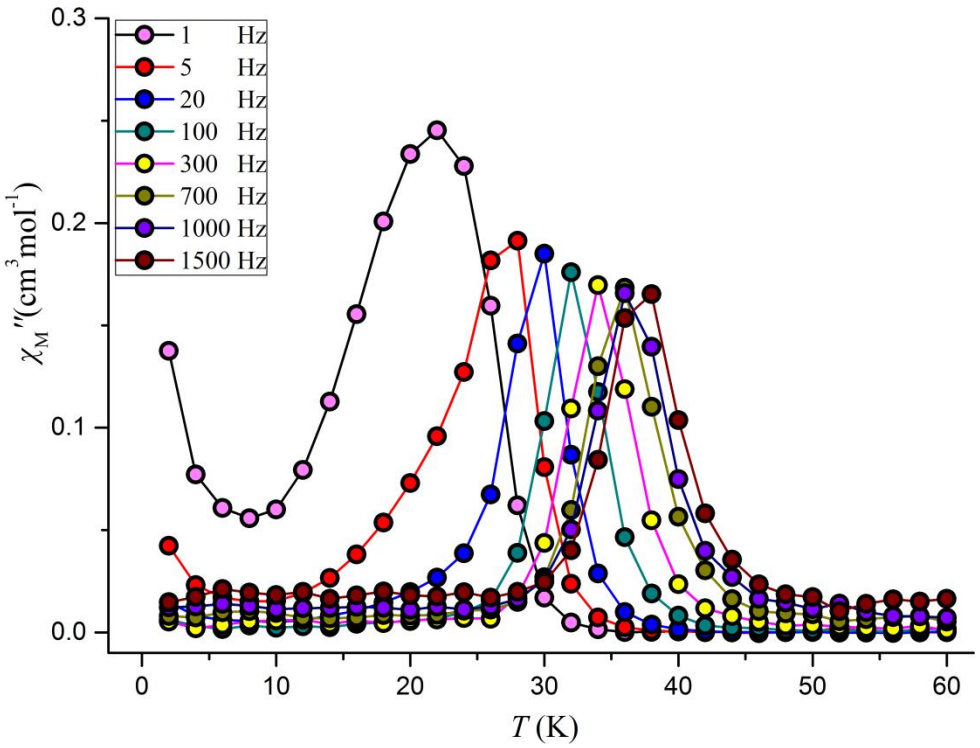

Fig. S22 Temperature dependence of the out-of-phase, χ''_M, product in zero dc field for **2** with ac frequencies of 1−1488 Hz.

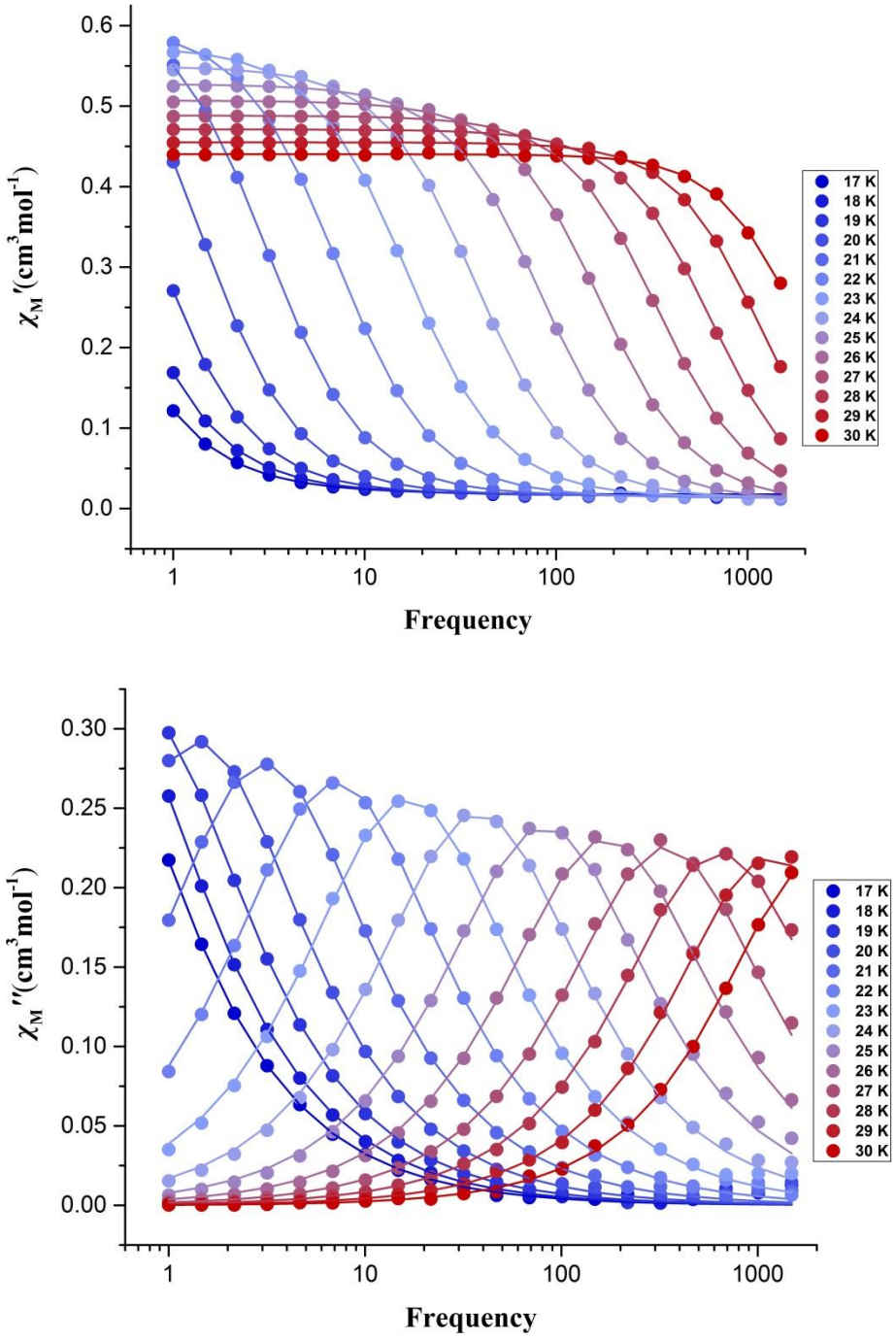

Fig. S23 (Top) Frequency dependent in-phase and (bottom) out-of-phase susceptibility signals for complex **1** in zero dc field, in the temperature range 17 – 30 K. The solid lines correspond to the best fit.

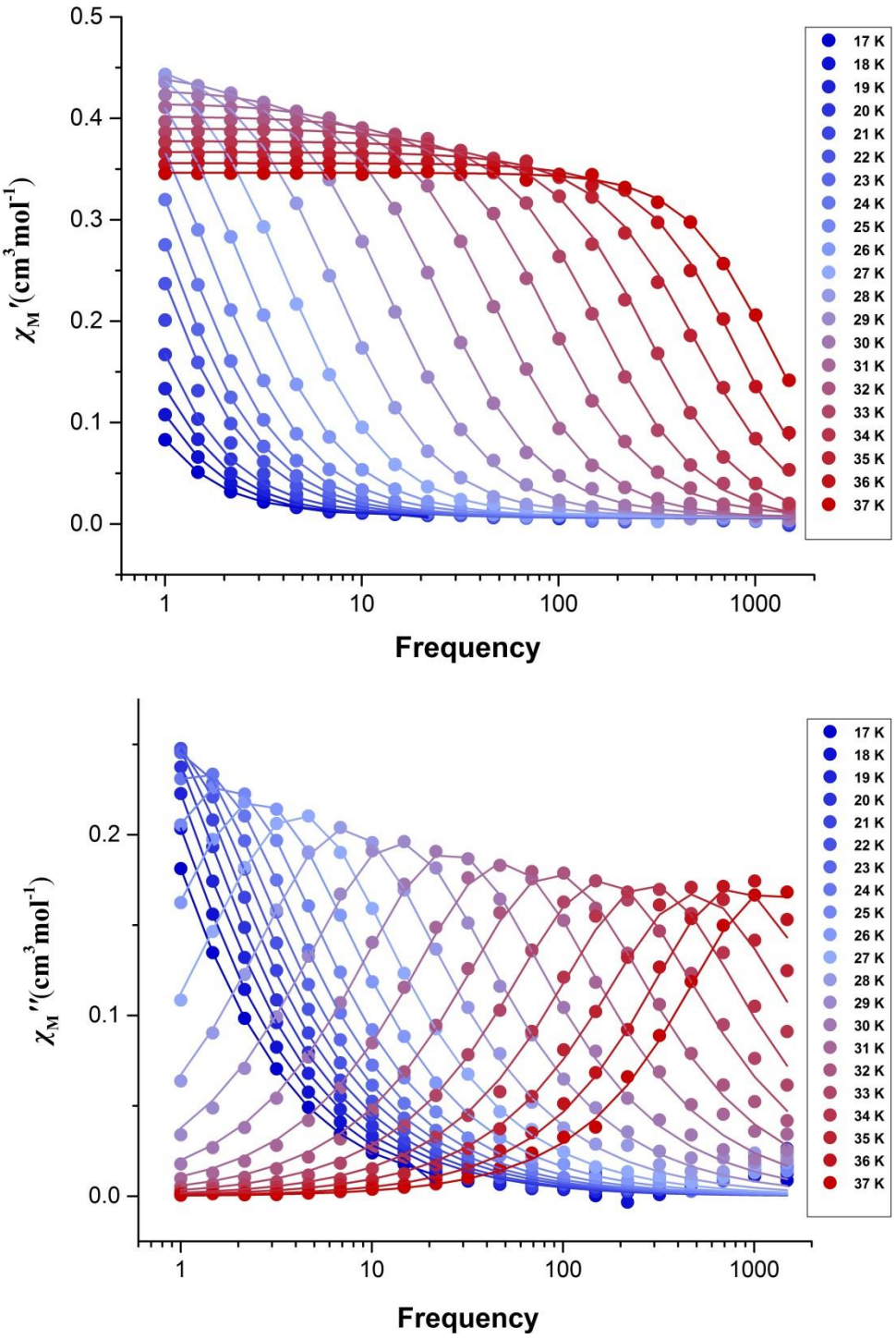

Fig. S24 (Top) Frequency dependent in-phase and (bottom) out-of-phase susceptibility signals for complex **2** in zero dc field, in the temperature range 17 – 37 K. The solid lines correspond to the best fit.

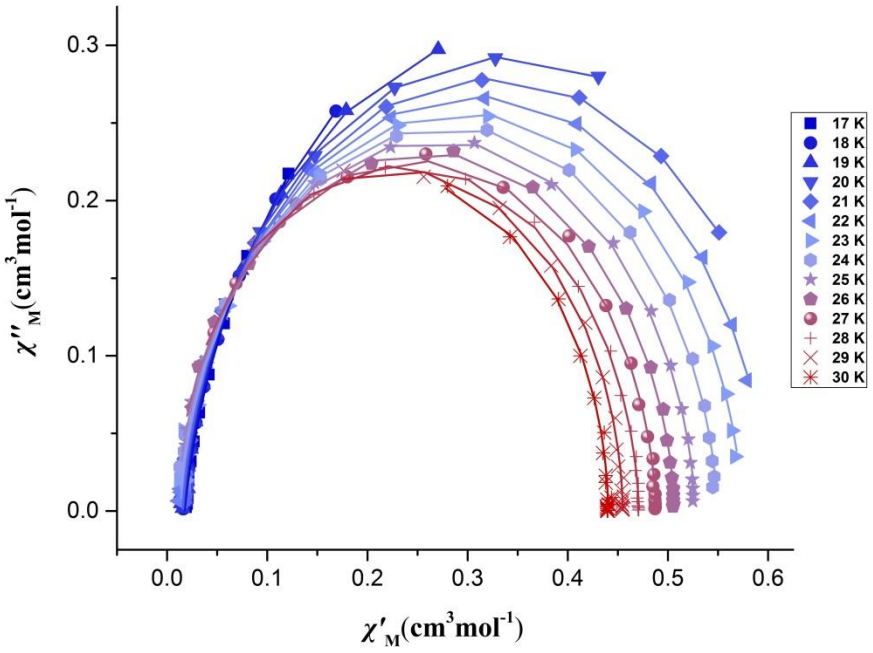

Fig. S25 χ''_M vs χ'_M plot of the AC magnetic susceptibility of **1** in zero dc field. The solid lines correspond to the best fit to Debye's law.

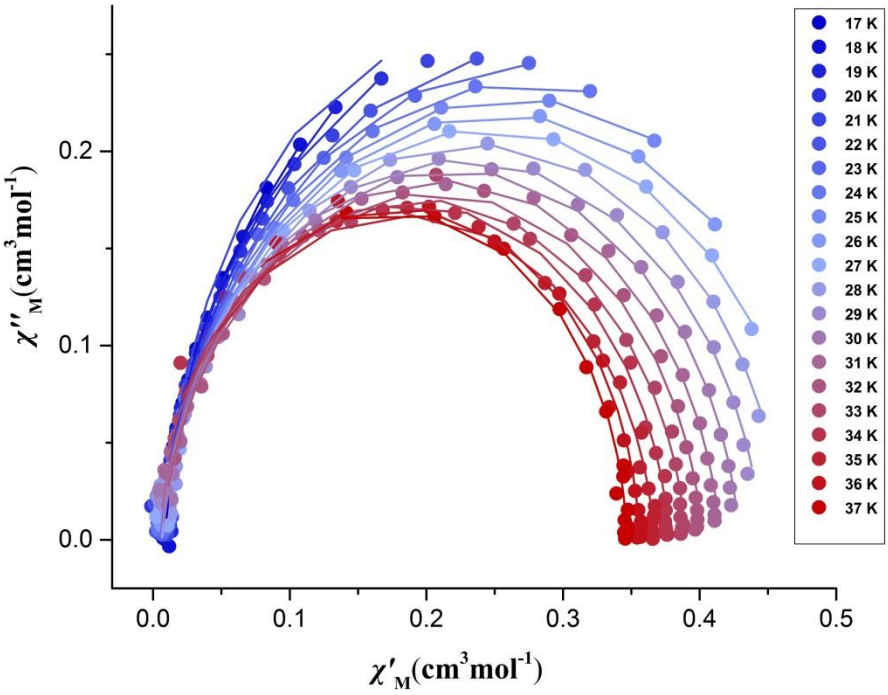

Fig. S26 χ''_M vs χ'_M plot of the AC magnetic susceptibility of **2** in zero dc field. The solid lines correspond to the best fit to Debye's law.

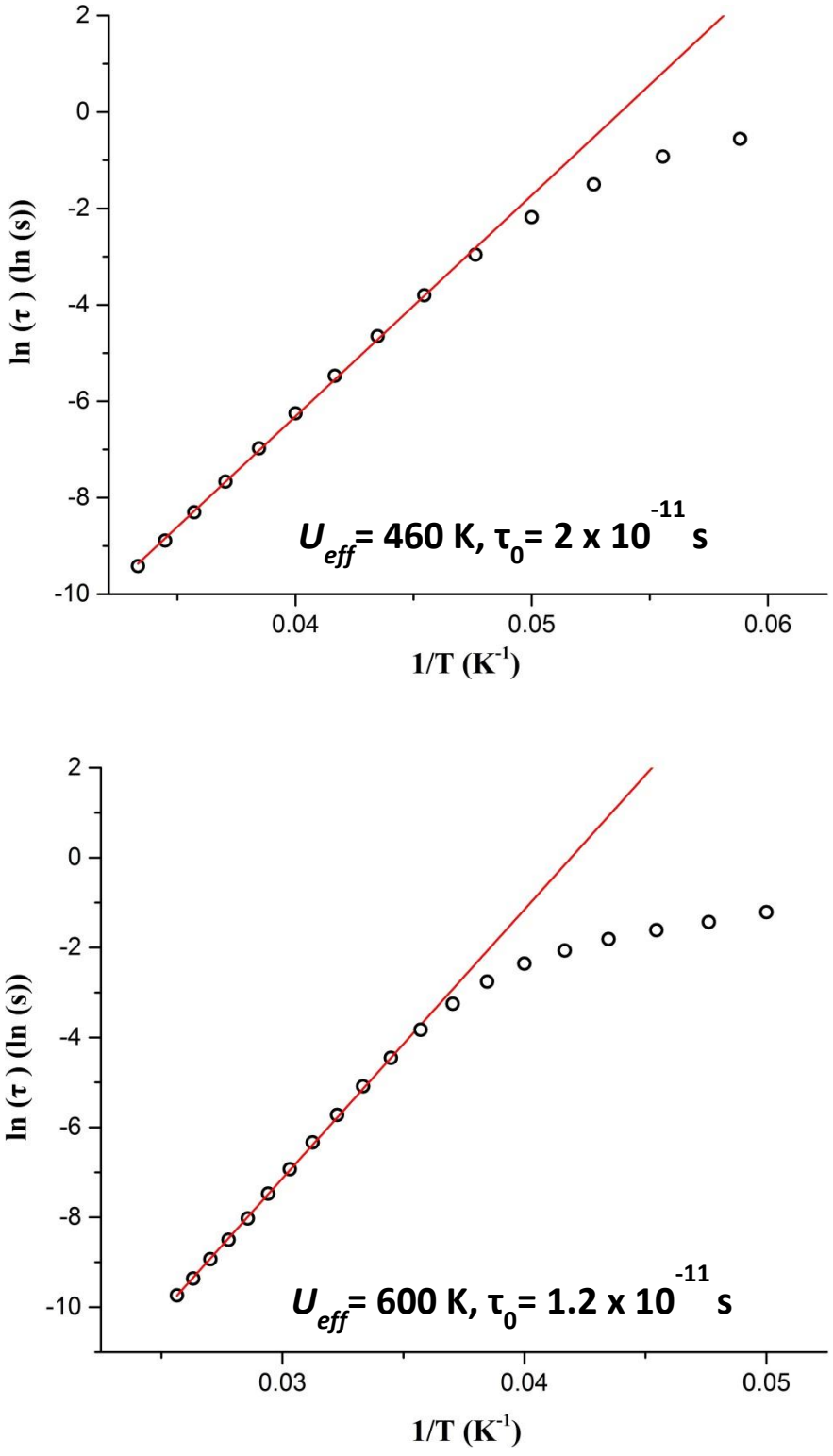

Fig. S27 Plot of the relaxation time τ (T) (logarithmic scale) versus T^{-1} for **1** (top) and **2** (bottom). The solid red line represents the best fit to the Arrhenius law.

Computational Details:

All the *ab initio* calculations have been performed using MOLCAS 8.0 code. Employed basis sets are given below.

C.ANO-RCC...3s2p.,
N.ANO-RCC...3s2p.,
O.ANO-RCC...4s3p2d1f.,
H.ANO-RCC...2s.,
P.ANO-RCC...4s3p.,
Cl.ANO-RCC...4s3p1d
I.ANO-RCC...6s5p2d.,
Dy.ANO-RCC...8s7p5d3f2g1h..

For the $4f^9$ electronic configuration of Dy(III), the $^6H_{15/2}$ multiplet is expected to be the ground state. In our first step, we have generated the guess orbitals. Then we have selected seven Dy(III) based starting orbitals to perform the CASSCF calculations. CASSCF calculations have been performed where eleven electrons are in the seven active orbitals with an active space of CAS(9,7). Using this active space first we have computed 21 sextets using the configuration interaction (CI) procedure. After this, we have performed RASSI-SO module to compute the spin-orbit coupled states. After computing these SO states, we have performed the SINGLE_ANISO code to extract the corresponding g-tensors. Here we have computed the g-tensors for the eight low-lying Kramers Doublets. The Cholesky decomposition for two electron integrals is employed throughout in the calculations to reduce the disk space.[5]

Analysis of qualitative relaxation mechanism: unlike in transition metal based SMMs/SIMs, in majority of lanthanide-based SMMs/SIMs, the thermally assisted magnetic relaxation occurs through TA-QTM (thermally assisted quantum tunneling of magnetization). Quenching TA-QTM at the first excited KD can cause relaxation via higher excited state(s) and increase the magnitude of U_{eff} values. Ungur and Chibotaru have proposed a methodology to derive the parameters that control the relaxation mechanism from the *ab initio* computed wave function. This involves calculation of the transition magnetic moment between the degenerate states of lanthanide-based SMMs. For Kramers doublets, the transition magnetic moment and tunneling rate (among the two degenerate states of a doublet) are proportional and the average sum of the transition magnetic moment, $((|\mu_x|+|\mu_y|+|\mu_z|)/3)$ qualitatively gives the transition probability between the two degenerate doublet states.[6]

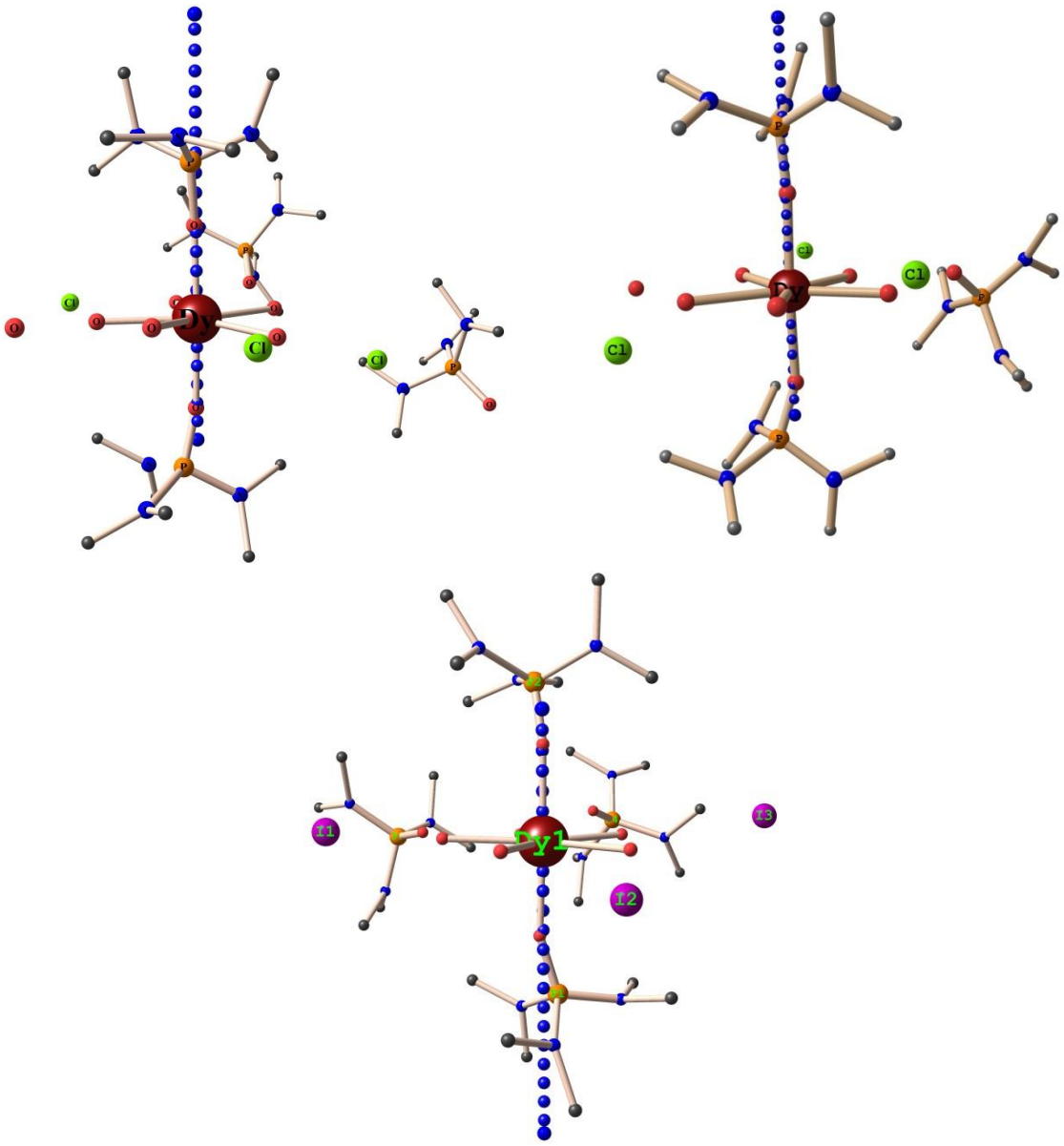

Fig. S28 *Ab initio* SINGLE_ANISO computed ground state KD orientations for complex **1** (upper left **1a** and upper right **1b**) and **2** (lower). Complex **1** has two crystallographic units (**1a** and **1b**) and calculations have been performed on both units. The computed g_{zz} axis for both the ground and first excited states is collinear in complexes **1** and **2** (less than 2°, see Table S6). The angle between the g_{zz} axis of the ground state KD and the other excited states is important as larger deviation from the ground state suggests a possibility of relaxation via that excited state. If the g_{zz} angle of the ground state and the first excited state align along the same direction (angle of deviation is zero), that means the g_{zz} axes are collinear. This collinearity is important for the

relaxation mechanism and collinearity here suggests that the g_{zz} axis of the two KDs are nearly aligned along the same direction.

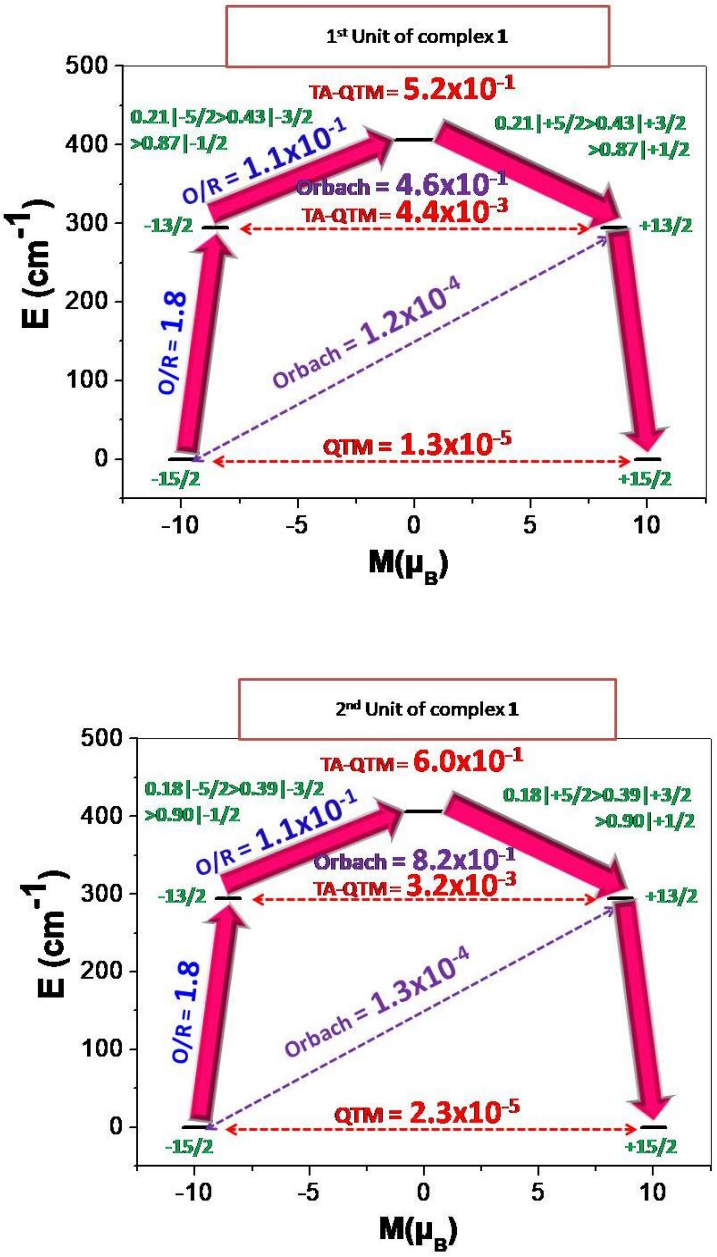

Fig. S29 *Ab initio* calculated relaxation dynamics for complex **1** (**1a** unit at top and **1b** unit at bottom). Relative energies are given in cm^{-1} and the arrows show the connected energy states with the number representing the matrix element of the transverse moment (see text in the manuscript for more details).

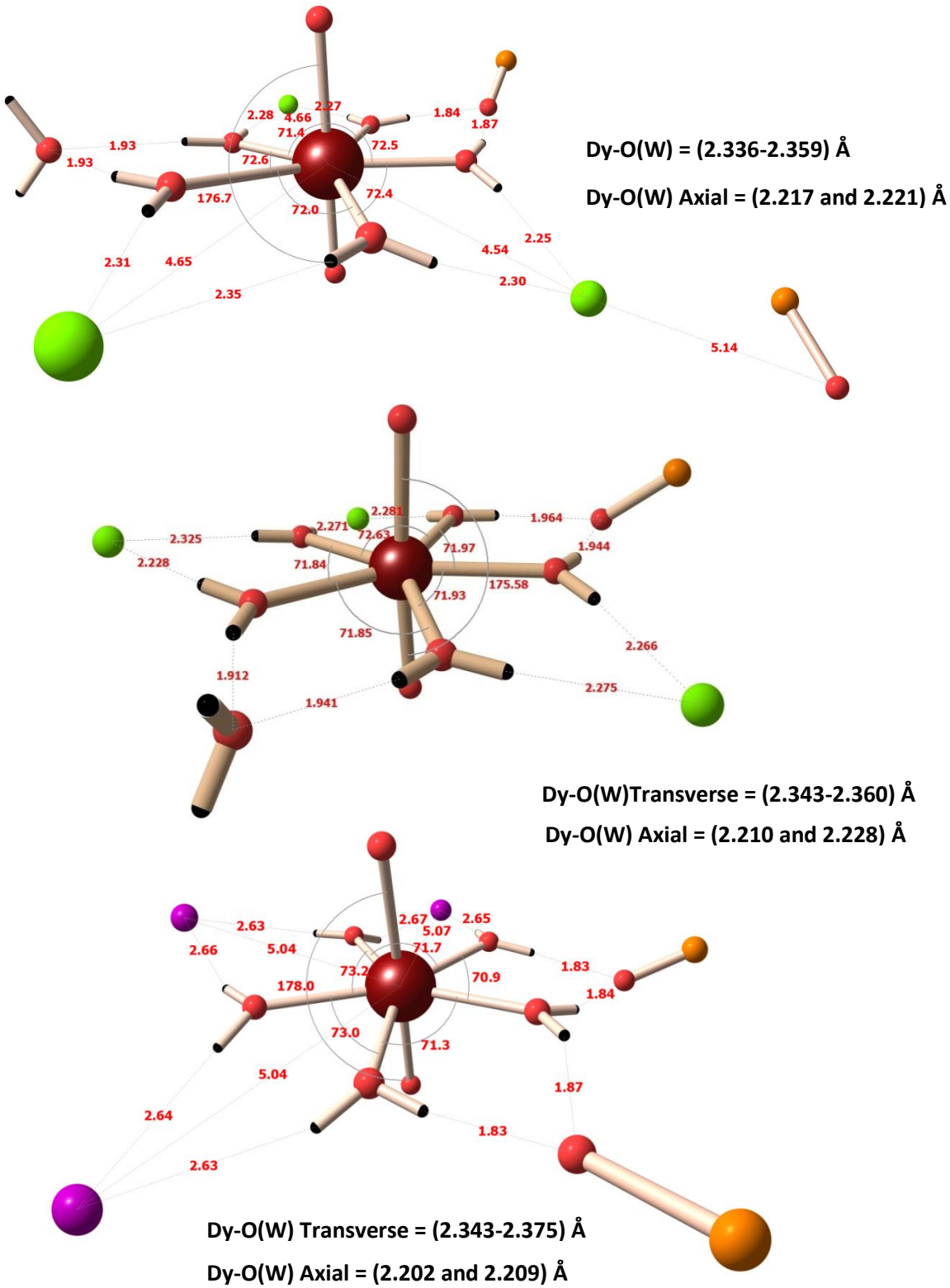

Fig. S30 Selected structural parameters for **1a** (top), **1b** (middle) and **2** (bottom).

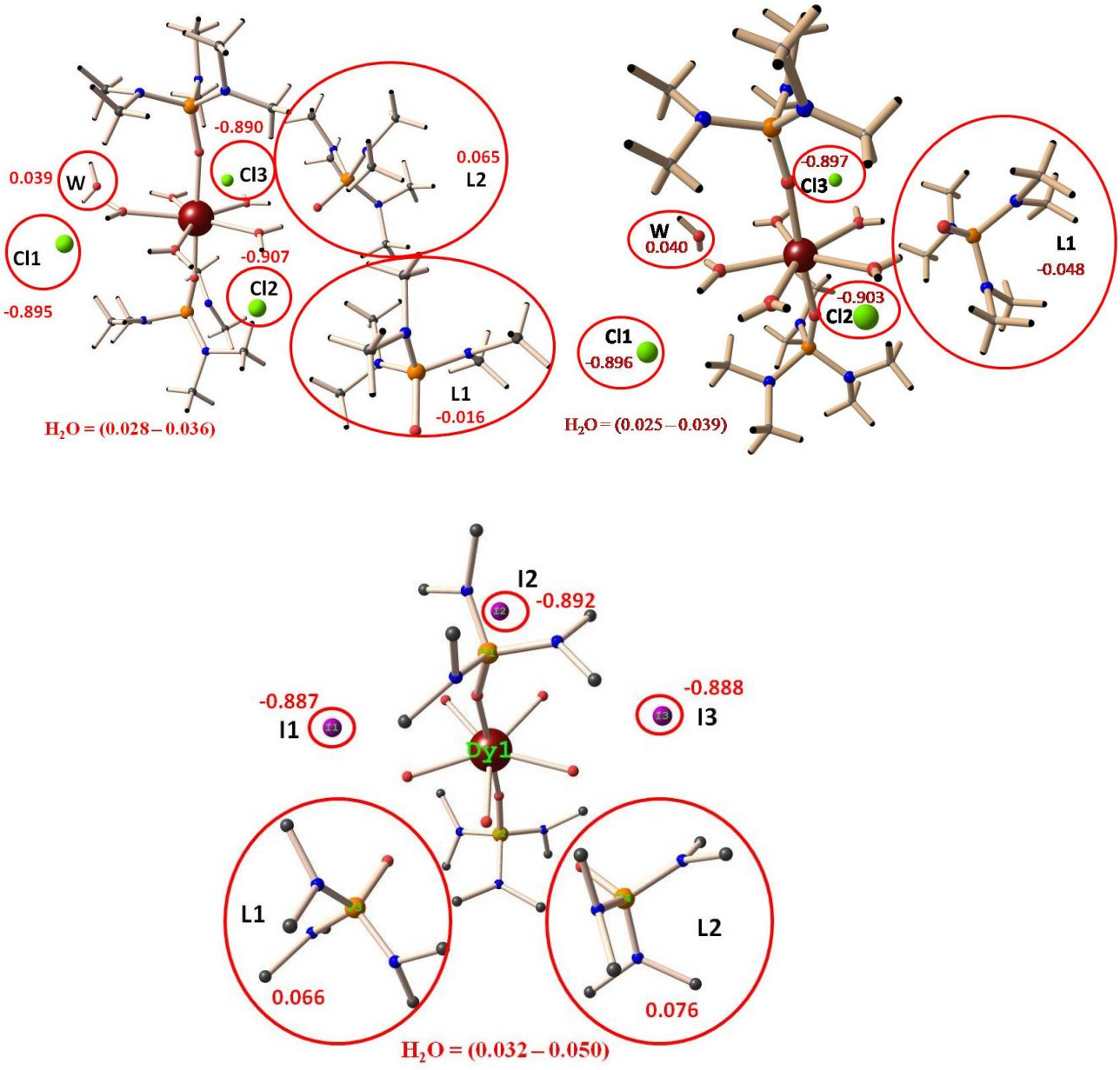

Fig. S31 *Ab initio* SINGLE_ANISO computed LoProp charges of fragments for complex **1** (**1a** upper left and **1b** upper right) and **2** (lower). On average, the charges on the Cl^- ions are found to be higher compared to the I^- ions, suggesting a larger transverse field contribution by the Cl^- ions to the Dy(III) ion with respect to the I^- ions. The LoProp charges are used to partition properties like dipole moments and polarizabilities into atomic and interatomic contributions.[7]

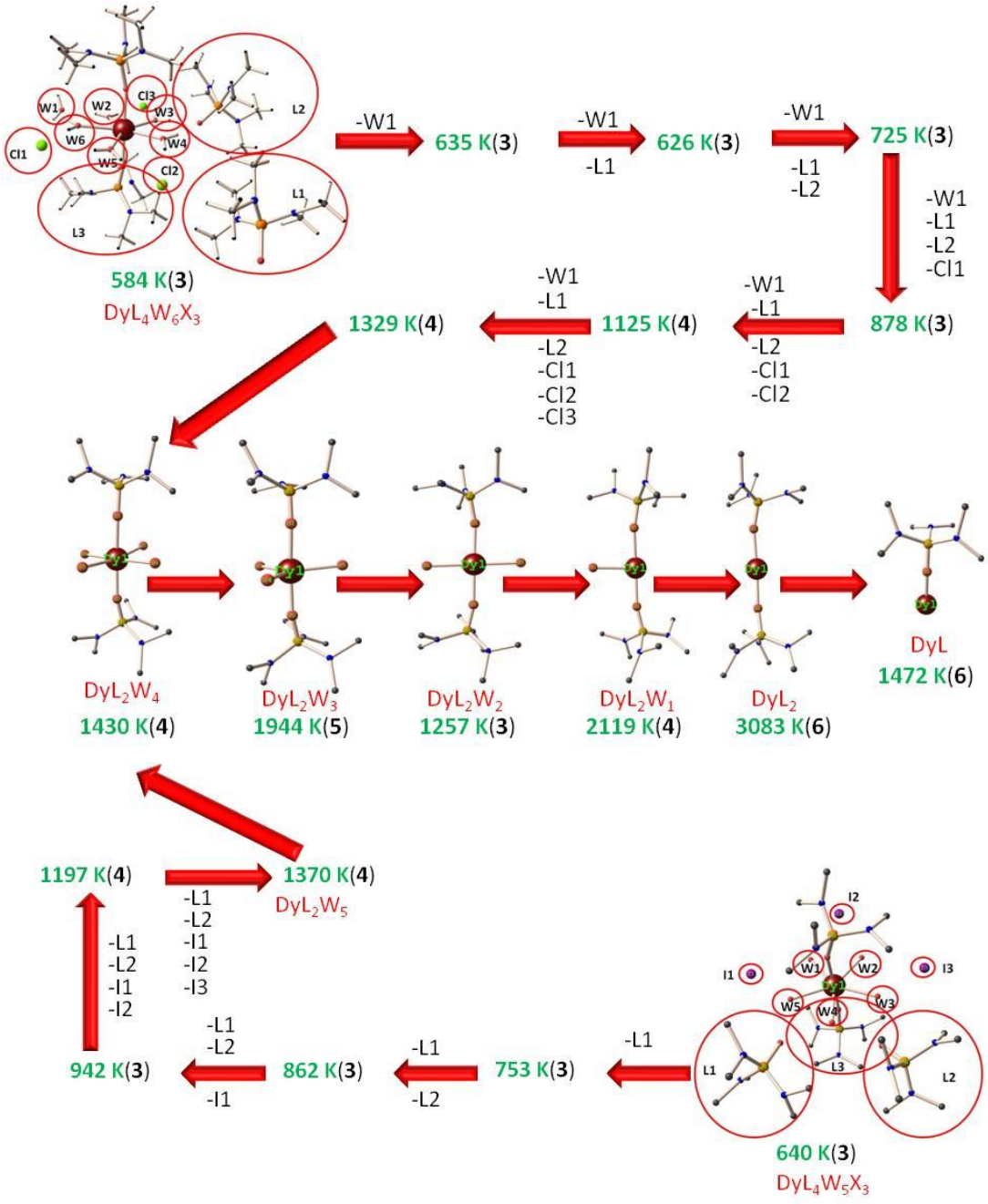

Fig. S32 *Ab initio* SINGLE_ANISO computed U_{cal} values for all the models created by removal of fragments one by one for complexes **1b** and **2**. Green color values show the U_{cal} value for each model. Numerical number in brackets for each model suggests the excited KD through which relaxation is expected (Ground state KD (1), first excited state KD (2) and so on).

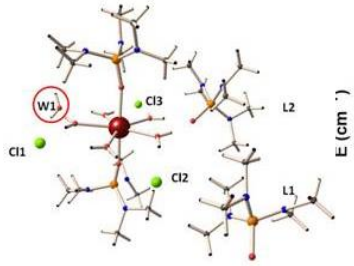

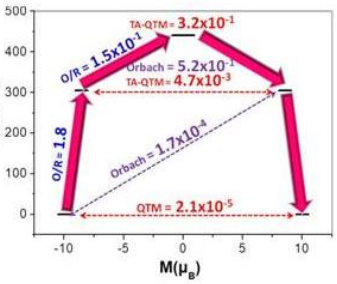

E cm-1	gxx	gyy	gzz	Angle
0.00	0.000	0.000	19.954	
305.07	0.012	0.016	17.056	1.6
440.95	0.441	1.149	18.640	92.5
503.89	2.544	3.035	10.806	34.9
530.86	3.276	5.195	7.243	32.2
578.24	7.962	4.316	0.148	109.7
630.33	1.419	2.745	15.548	55.0
650.98	0.160	1.391	17.107	59.6

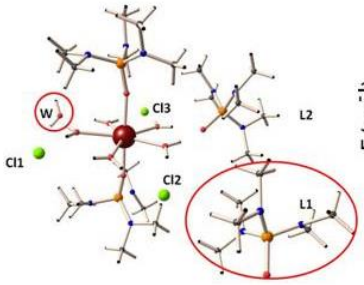

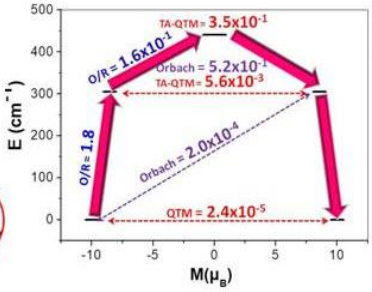

E cm-1	gxx	gyy	gzz	Angle
0.00	0.000	0.000	19.953	
303.10	0.014	0.019	17.053	1.6
435.30	0.463	1.253	18.562	92.5
498.63	3.060	3.387	10.392	39.2
524.42	3.258	4.516	7.866	27.8
571.32	0.399	3.991	7.931	22.0
624.58	1.403	3.042	15.251	54.4
644.27	0.059	1.491	17.047	59.3

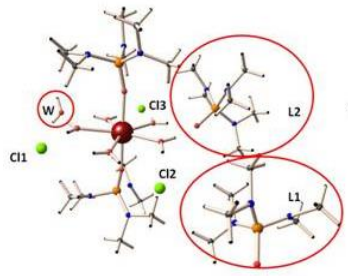

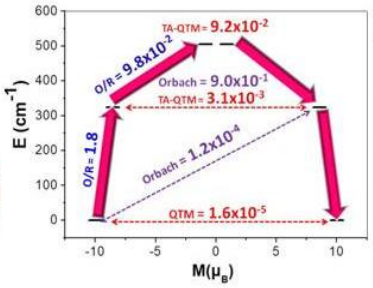

E cm-1	gxx	gyy	gzz	Angle
0.00	0.000	0.000	19.962	
323.97	0.008	0.010	17.063	1.4
504.42	0.015	0.352	18.354	95.5
552.41	0.145	0.631	12.478	14.0
600.28	2.555	5.266	11.031	95.9
641.58	2.943	4.732	8.242	26.2
697.20	0.982	1.582	16.521	59.4
724.35	0.039	1.135	17.847	62.7

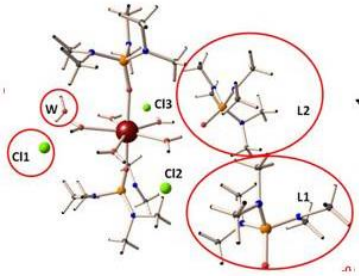

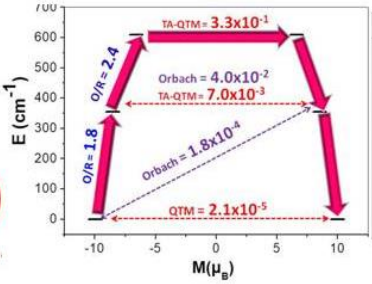

E cm-1	gxx	gyy	gzz	Angle
0.00	0.000	0.000	19.954	
355.39	0.020	0.022	17.068	1.0
610.00	0.463	1.295	13.397	8.7
668.59	0.099	3.056	15.725	94.7
712.44	2.405	3.512	12.284	88.9
755.85	7.081	5.208	0.355	73.5
774.78	2.429	4.837	9.253	48.4
811.52	2.049	3.967	13.485	59.0

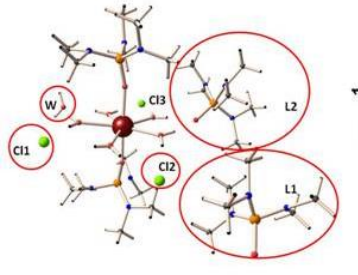

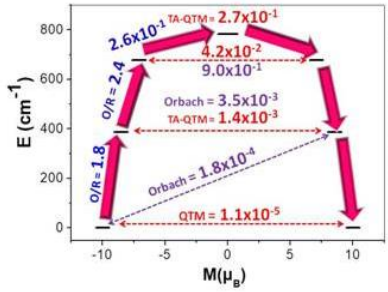

E cm-1	gxx	gyy	gzz	Angle
0.00	0.000	0.000	19.977	
387.92	0.004	0.004	17.082	0.6
676.98	0.091	0.158	14.199	2.6
782.37	0.347	1.004	18.212	91.5
827.81	3.554	4.306	11.002	96.1
857.86	1.389	3.168	10.288	60.7
899.53	0.684	3.408	14.230	69.8
920.36	1.313	3.773	13.138	59.2

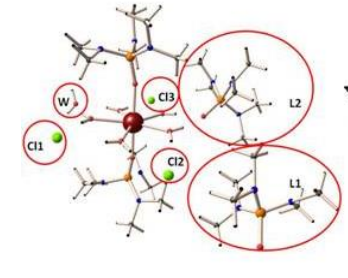

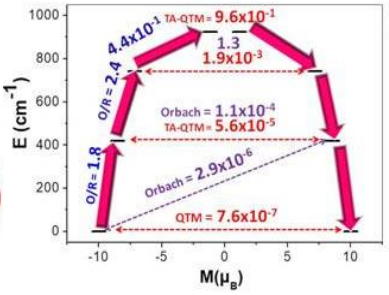

E cm-1	gxx	gyy	gzz	Angle
0.00	0.000	0.000	19.979	
419.84	0.000	0.000	17.073	0.4
740.53	0.006	0.006	14.311	0.8
924.04	1.625	3.589	13.443	99.9
936.79	0.947	3.766	8.338	10.9
962.77	5.778	4.879	2.137	67.5
1001.69	0.971	3.689	8.393	40.0
1013.70	1.909	2.573	11.208	40.9

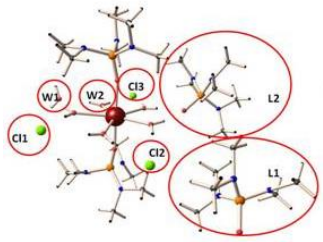

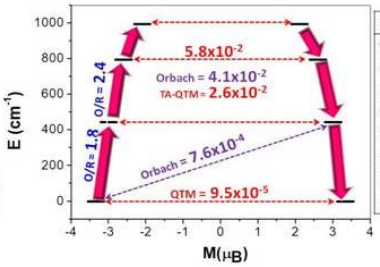

E cm-1	gxx	gyy	gzz	Angle
0.00	0.000	0.000	19.955	
443.11	0.076	0.078	16.915	2.5
794.75	0.064	0.249	13.528	6.0
993.78	8.314	7.260	5.977	21.6
1125.4	0.326	0.745	15.950	97.2
1150.1	0.022	2.036	14.435	93.8
1266.8	0.297	1.032	17.371	84.7
1300.1	0.550	1.623	18.138	84.7

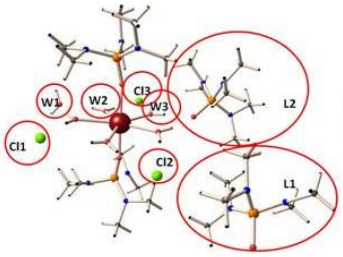

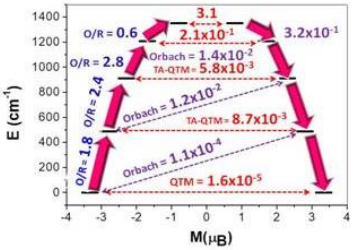

E cm-1	gxx	gyy	gzz	Angle
0.00	0.000	0.000	19.993	
488.8	0.026	0.026	17.042	0.7
910.6	0.010	0.022	14.172	1.5
1210.3	0.557	0.644	10.970	3.7
1351.5	9.206	8.599	4.483	7.1
1403.0	0.685	3.894	15.310	89.8
1430.7	1.419	2.687	9.946	90.4
1464.5	1.414	4.475	13.890	82.1

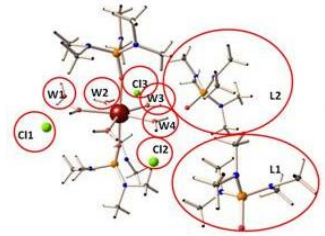

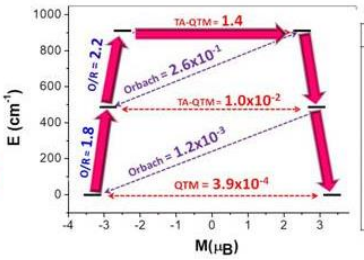

E cm-1	gxx	gyy	gzz	Angle
0.00	0.000	0.000	19.993	
507.9	0.025	0.036	16.759	2.8
874.1	1.952	4.945	11.285	25.3
1006.5	7.742	6.616	1.628	8.6
1250.1	1.716	2.696	11.172	90.0
1603.4	0.174	0.281	14.506	90.2
1993.3	0.074	0.112	17.103	90.4
2208.0	0.013	0.024	19.768	90.7

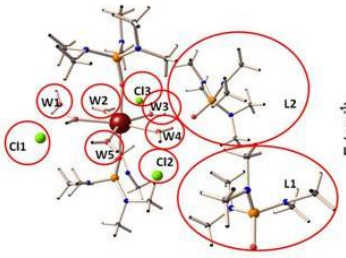

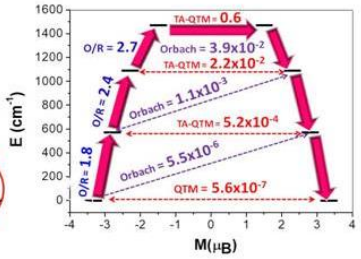

E cm-1	gxx	gyy	gzz	Angle
0.00	0.000	0.000	19.993	
572.7	0.001	0.002	16.941	0.5
1092.9	0.059	0.070	13.961	1.3
1473.0	1.104	2.127	10.200	5.4
1619.8	2.891	6.571	10.526	91.7
1790.8	1.111	1.993	13.026	90.2
2019.3	0.022	0.137	16.670	90.3
2164.6	0.065	0.101	19.673	90.5

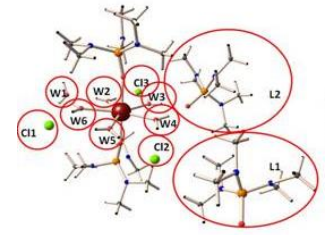

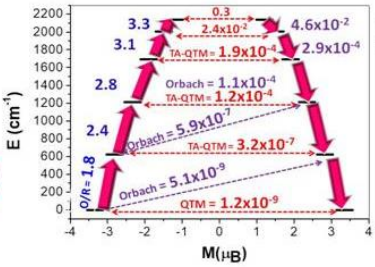

E cm-1	gxx	gyy	gzz	Angle
0.00	0.000	0.000	20.012	
624.7	0.000	0.000	16.976	0.2
1214.2	0.000	0.000	14.069	0.2
1696.4	0.000	0.001	11.406	0.0
2004.9	0.070	0.073	8.958	1.1
2142.9	0.666	0.906	6.488	7.6
2178.2	11.532	7.895	2.118	3.0
2188.9	0.516	2.256	17.768	89.1

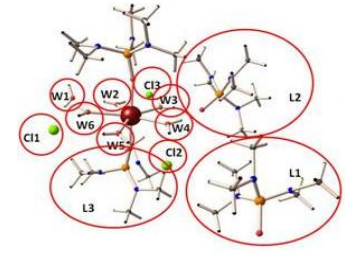

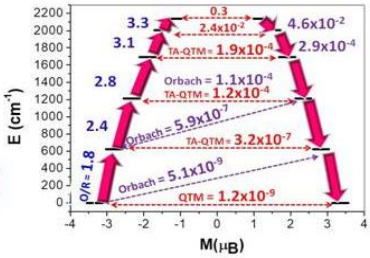

E cm-1	gxx	gyy	gzz	Angle
0.00	0.000	0.000	20.010	
319.3	0.000	0.000	17.178	0.7
590.8	0.001	0.001	14.429	1.0
798.6	0.000	0.001	11.768	1.5
939.3	0.045	0.047	9.162	2.7
1022.7	0.865	1.016	6.542	5.4
1065.4	3.605	3.932	5.281	82.4
1085.0	1.068	5.671	14.872	91.0

Fig. S33 *Ab initio* SINGLE_ANISO computed U_{cal} values (in cm^{-1}) for all the models created by removal of fragments one by one for complex **1b**. Left: Model molecular structure, Middle: Model relaxation blockade barrier diagram and Right: Table with KDs energy, g tensors and angles of excited KDs with respect to ground state KD. It should be noted that those fragments which are close to the first coordination sphere have a considerable effect on the U_{cal} value and those which interact with the second coordination sphere have a very small effect on the U_{cal} values. For example L1 in complex **1b** is weakly interacting with the second coordination sphere resulting in no major change in the U_{cal} value.

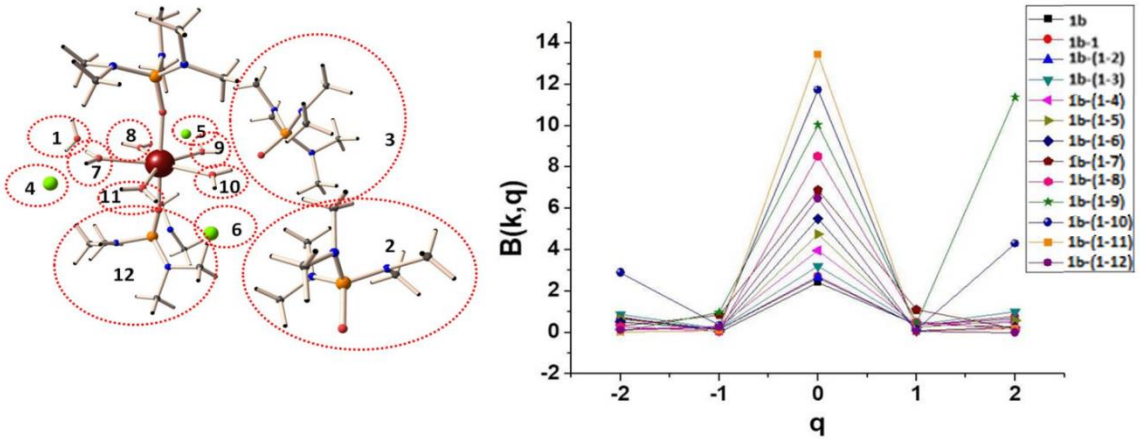

Fig. S34 *Ab initio* SINGLE_ANISO computed crystal field parameters for all the models created by removal of fragments one by one for complex **1b** (right). **1b** represents the complete complex and minus numbers after that represent fragment number(s) removed from the complex. Pictorial presentation of sequential removals of fragments (left). Numbers represent the sequence in which fragments are being removed.

References

1. O. V. Dolomanov et al., *J. Appl. Cryst.*, 2009, **42**, 339.
2. Sheldrick, G. M. (2008). *Acta Cryst.* A**64**, 112–122.
3. Sheldrick, G. M. (2015). *Acta Cryst.* A**71**, 3–8.
4. M. Llunell, D. Casanova, J. Cirera, P. Alemany and S. Alvarez, Shape Program, Version 2.0, 2010
5. a) F. Aquilante, J. Autschbach, K. Carlson Rebecca, F. Chibotaru Liviu, G. Delcey Mickaël, L. De Vico, I. Fdez. Galván, N. Ferré, M. Frutos Luis, L. Gagliardi, M. Garavelli, A. Giussani, E. Hoyer Chad, G. Li Manni, H. Lischka, D. Ma, Å. Malmqvist Per, T. Müller, A. Nenov, M. Olivucci, B. Pedersen Thomas, D. Peng, F. Plasser, B. Pritchard, M. Reiher, I. Rivalta, I. Schapiro, J. Segarra-Martí, M. Stenrup, G. Truhlar Donald, L. Ungur, A. Valentini, S. Vancoillie, V. Veryazov, P. Vysotskiy Victor, O. Weingart, F. Zapata and R. Lindh, *J. Comput. Chem.,* 2015, **37**, 506-541; b) F. Aquilante, L. De Vico, N. Ferré, G. Ghigo, P.-å. Malmqvist, P. Neogrády, T. B. Pedersen, M. Pitoňák, M. Reiher, B. O. Roos, L. Serrano-Andrés, M. Urban, V. Veryazov and R. Lindh, *J. Comput. Chem.,* 2010, **31**, 224-247; c) J. A. Duncan, *J. Am. Chem. Soc.,* 2009, **131**, 2416-2416; d) V. Veryazov, P. O. Widmark, L. Serrano-Andrés, R. Lindh and O. Roos Björn, *Int. J. Quantum Chem.,* 2004, **100**, 626-635; e) G. Karlström, R. Lindh, P.-Å. Malmqvist, B. O. Roos, U. Ryde, V. Veryazov, P.-O. Widmark, M. Cossi, B. Schimmelpfennig, P. Neogrady and L. Seijo, *Comput. Mater. Sci.,* 2003, **28**, 222-239; f) L. F. Chibotaru and L. Ungur, *J. Chem. Phys.,* 2012, **137**, 064112; g) F. Habib, R. Luca Oana, V. Vieru, M. Shiddiq, I. Korobkov, I. Gorelsky Serge, K. Takase Michael, F. Chibotaru Liviu, S. Hill, H. Crabtree Robert and M. Murugesu, *Angew. Chem. Int. Ed.,* 2013, **52**, 11290-11293; h) S. K. Langley, L. Ungur, N. F. Chilton, B. Moubaraki, L. F. Chibotaru and K. S. Murray, *Inorg. Chem.,* 2014, **53**, 4303-4315. I) B. O. Roos, R. Lindh, P.-Å. Malmqvist, V. Veryazov, P.-O. Widmark and A. C. Borin, *J. Phys. Chem. A* 2008, **112,** 11431-11435.
6. L. Ungur, M. Thewissen, J. P. Costes, W. Wernsdorfer and L. F. Chibotaru, *Inorg. Chem.*, 2013, **52**, 6328.
7. L. Gagliardi, R. Lindh and G. Karlström, *J. Chem. Phys.*, 2004, **121**, 4494-4500.